A double-layer iterative analytical model for mesh stiffness and load distribution of early-stage cracked gear based on the slicing method

Lantao Yang[1], Liming Wang[1*], Yimin Shao[1], Fengshou Gu[2], Andrew Ball[2], David Mba[3*]

[1] State Key Laboratory of Mechanical Transmission, Chongqing University, Chongqing 400044, China

[2] Centre for Efficiency and Performance Engineering, University of Huddersfield, Huddersfield HD1 3DH, UK

[3] Creative Computing Institute, University of the Arts London, London WC1V 7EY, UK

[*]Corresponding author. E-mail address: lmwang@cqu.edu.cn; d.mba@arts.ac.uk

Abstract: To reveal the coupling relationship between the time-varying mesh stiffness (TVMS) and the load distribution along the tooth width direction (TWD) of gears with early-stage crack (ESC), a double-layer iterative analytical model for the TVMS and load distributions of gears is proposed considering the effects of the non-uniformly distributed load (NDL) along TWD caused by the ESC. In the proposed model, an analytical model of tooth torsional deformation and a parallel slice stiffness model of the tooth pair with ESC are separately developed based on the slicing method. On this basis, a double-layer iterative calculation method for the TVMS and load distributions is proposed, in which the coupling relationships between the slice stiffness and load distribution along TWD as well as the TVMS and load distribution between the meshing tooth pairs are respectively presented with the inner- and outer- layer iterations. Finite element (FE) models are established to verify the proposed double-layer iterative model. The effects of crack parameters and applied torque on the tooth torsional deformation, TVMS, and load distributions of the gear with ESC are finally investigated based on the proposed model. The results show that the proposed model can realize the accurate and fast decoupling calculation of the TVMS and load distributions of gears with ESC. This study can provide a basis for the establishment of the refined ESC fault diagnosis method and the rapid evaluation of the load distributions of gears with asymmetric errors or faults along TWD.

Keywords: Gear fault diagnosis; Mesh stiffness; Load sharing factor; Early-stage crack; Slice method

Nomenclature	
subscript i	Subscript i = 1, 2, 3 represents Zone *I* (i = 1), *II* (i = 2) or *III* (i = 3), respectively
subscript j	Subscript j denotes the jth slice along TWD
subscript λ	Subscript λ refers to the health ($\lambda = h$) or crack ($\lambda = c$)
subscript κ	Subscript κ means the κth meshing tooth pair
α_1	Meshing force angle
α_2	Half of the central angle corresponding to the base circle
$A_{\lambda x i}$	The area of the micro-section dx_i of the tooth slice
d_i	The horizontal distance of the micro-section dx_i
E	The Elasticity modulus of gears
E_κ	The backlash of the κth meshing tooth pair
E_F	The loaded static transmission error of gears
F	Meshing force
F_λ	Meshing force of healthy ($\lambda = h$) /cracked ($\lambda = c$) tooth pair
F_κ	Meshing force of the κth meshing tooth pair
$\mathbf{F_s}$	Meshing force vector of slices
F_{sj}	Meshing force of the jth slice

|	
$F_a, F_b /F_{aj}, F_{bj}$	Axial compression and shear forces decomposed by meshing force F/F_{sj}
G	Shear modulus of gears
h_1	Half tooth height at the meshing point position
$h_{F(xi)}$	The effective moment arm of F_{aj}
h_r	The vertical distance between the intersections of the addendum circle and tooth profile and the tooth centerline
h_{cxi}	The length of the effective micro-section dx_i of the cracked tooth
h_{qxi}	Height of dead zone shown in Fig. 6
$I_{\lambda xi}$	Area of inertia of the micro-section dx_i of the slice
$I_{pxi (\lambda)}$	The polar moment of inertia of the healthy ($\lambda = h$) /cracked ($\lambda = c$) tooth
$k_{b\lambda j}/k_{s\lambda j}/k_{a\lambda j}/k_{f\lambda j}$	Stiffness of bending/shear/axial compression/fillet foundation of the jth slice
$k_{cj(j+1)}$	Coupling stiffness between the jth and (j+1)th slices
k_{hj}	Contact stiffness
$k_{t\lambda j}$	Torsional stiffness of the jth slice of the healthy ($\lambda = h$) /cracked ($\lambda = c$) tooth
$k_{t\_e\lambda j}$	Stiffness of the jth slice of the healthy ($\lambda = h$) /cracked ($\lambda = c$) tooth in the tooth pair with ESC
k_{tp_hj}	TVMS of slice pairs of the healthy tooth pair
k_{tpj}	TVMS of slice pairs of the tooth pair with ESC
K_{ec_single}	TVMS of the tooth pair with ESC
K_{h_single}	TVMS of the healthy tooth pair
K_t	TVMS of the gear with ESC
$K_{t(FE)}$	TVMS of the gear obtained by the FE model
$\mathbf{K_C}$	Stiffness matrix of slices considering slice coupling effect
$\mathbf{K_{CP}/K_{CG}}$	Stiffness matrix of slices of cracked/healthy tooth considering slice coupling effect
$\mathbf{K_{CH}}$	Contact stiffness matrix of meshing slice pair
$\mathbf{K_{tp}}$	Stiffness vector of meshing slice pair considering slice coupling effect
l	The effective moment arm of F_{bj3} on the micro-section dx_3
LSF_{tp}/LSF_{tw}	Load sharing factor between tooth pairs/along TWD
$LSF_{tp\kappa}/LSF_{twj}/LSF_{twj(FE)}$	LSF_{tp} of the κth meshing tooth pair/LSF_{tw} of the jth slice pair/LSF_{tw} of the jth slice pair obtained by the FE model
m	Modulus of gear
n	Number of slices
q_0	Maximum depth of ESC
$q(z)$	The crack depth corresponding to the position z_j along TWD
Q_κ	The deformation of the κth tooth pair under unit force
$R_a/R_b/R_g$	Radius of addendum/base/dedendum circles
S_j	Total stress distribution area of the jth tooth slice region
S_a/S_r	The backlash of the tooth pairs mesh in advance or mesh out in delay
T_p	Applied torque on the driving gear
$T_{t(\lambda)}$	Tooth torsional moment of the healthy ($\lambda = h$) /cracked ($\lambda = c$) tooth
$U_{bhj}/U_{shj}/U_{ahj}$	Deformation energy of bending/shear/axial compression of the jth slice
$W/\Delta W$	Width of the tooth/slice

W_c	Crack length along TWD
x_i	Tooth profile position of the effective micro-section dx_i
$\Delta z/\Delta y$	The offset distance of O_1 related to the Y and Z axes in the coordinate YO_0Z in Fig. 6
Z_F	The equivalent moment arm of the tooth load around the section center O_1 in Fig. 6
β	*D*ecomposition angle of mesh force in Zone *III*
δ/δ_j	Total deformation of the tooth pair/jth slice
$\delta_{t\lambda j}$	Torsional deformation of the jth slice of the healthy ($\lambda = h$) /cracked ($\lambda = c$) tooth
δ_t	Deformation vector of slices
θ	Position angle of the effective micro-section dx_3
θ_f	Half of the tooth angle corresponding to the dedendum circle
$\Delta\theta_f$	Torsional deformation angle of the gear body under torque T_p
φ_λ	Torsional deformation angle of loaded tooth cross-section of the healthy ($\lambda = h$) /cracked ($\lambda = c$) tooth
v	Crack angle
γ	Attachment angle of the cantilever beam of the cracked tooth
σ_j	Total stress of the jth tooth slice region
Abbreviations	
TVMS	Time-varying mesh stiffness
FE	Finite element
NDL	Non-uniformly distributed load
TWD	Tooth width direction
ESC	Early-stage crack
ETC	Extended tooth contact

1. Introduction

Gear is one of the key components of the gear transmission system, which is widely used in various equipment in daily life [1, 2]. Due to the periodic load excitation on the tooth surface or the gear overload, the gear tooth is prone to crack. With the ESC propagation, the tooth or the body (rim) of gears will be broken, finally leading to catastrophic accidents [3, 4]. Therefore, it is of great academic and engineering value to study and establish the fault diagnosis method and the rapid evaluation of the load distribution of the gears with ESC fault.

The generation of cracks will change the internal excitation characteristics of gears and affect the gear vibration characteristics. Establishing an accurate analytical model of the internal excitation of cracked gear has become one of the most popular topics for studying the vibration characteristics of crack faults [5, 7]. The early analytical models of the internal excitation of cracked gear mainly focused on the through-crack style, that is, the crack is assumed to run through the whole tooth width and the depth is equal along the TWD. According to the propagation path direction, through-cracks can be divided into two types: tooth cracks and body cracks [8, 9], which are displayed in Fig. 1. At present, the internal excitation modelling of tooth crack cases has been extensively studied compared to the body crack [10]. The existing tooth crack models all assume that the crack will reduce the tooth attachment area on the gear body [11] and the effective load-bearing tooth thickness [12], and then lead to the decline of the

TVMS excitation. Therefore, previous studies [13-18] mainly focused on the influence of changes in the tooth attachment area and the effective load-bearing tooth thickness caused by different crack parameters (crack depths, angles and shapes etc.) and different types of limiting lines (horizontal lines, oblique lines and parabolas etc.) of the load-bearing tooth thickness on the TVMS. For the body cracked gear, Zhou [19] proposed a semi-planar cantilever beam model to study the influence of body crack growth on the TVMS excitation, but this model will overestimate the TVMS since it does not meet the ideal cantilever beam hypothesis [20]. Yang et al. [21-22] believed that the propagation of the body crack would cause changes in both the area and angle of the tooth cantilever beam attached to the body foundation. By redefining a new cantilever beam model of the cracked tooth, they investigated the effects of the crack parameters on the fillet foundation stiffness and TVMS of the cracked gear.
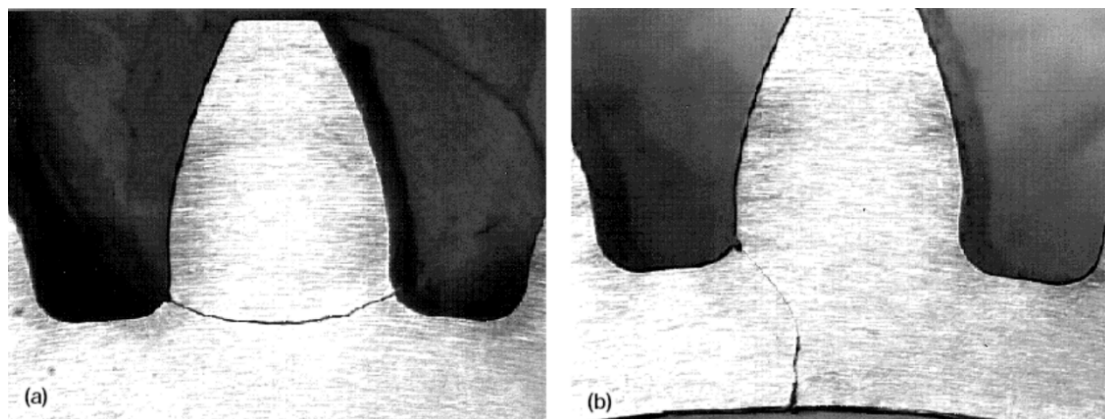
Fig. 1. Crack propagation paths [8-9]: (a) tooth crack, (b) body crack.

Due to shaft misalignment, tooth material defects and other factors, the early-stage cracks usually do not run through the whole tooth width but are non-uniformly distributed along the TWD [23]. In 2011, Chen and Shao [24] assumed the crack as a parabolic shape along the TWD and then proposed the so-called "slicing method" based on the integral idea to calculate the TVMS of gears with ESC. Later, the model in Ref. [24] was widely used to calculate the internal excitation of gears with ESC and was also continuously improved by many scholars. For example, Mohammed [13] and Chen et al. [14] used the slicing method to study the influences of the limiting line type of the effective tooth-bearing thickness on the TVMS of the gears with ESC. Mohammed [25] studied the effect of the initial crack propagation on gear TVMS based on the slicing method. Yang et al. [26] established a TVMS analytical model of the gear with ESC by using the slicing method and studied the effects of crack propagation on the TVMS considering the clearance nonlinearity. The slicing method provides an effective and convenient means for the TVMS calculation modelling of gears with non-uniformly distributed stiffness along TWD and has been widely used by scholars in other areas, such as the TVMS modelling of gears with installation or machining errors [27, 28], spalling [29] and wear [30] faults and so on. However, due to the non-uniformly distributed tooth stiffness along the TWD of the gears with ESC, the load distributions along TWD also show non-uniform characteristics, which will inevitably cause additional torsional deformation of the tooth pair with ESC, and then affect the TVMS excitation. While in the traditional TVMS calculation models [13,14, 23-26] of gears with ESC, the tooth torsional deformation caused by the NDL along TWD is ignored. In addition, the existing formulas in [31, 32] for calculating the tooth torsional deformation are all based on the energy method and can only calculate the equivalent deformation of the whole tooth under the assumption of a specific load distribution, which will inevitably cause calculation errors and can not obtain the actual tooth torsional deformation of specific positions

along TWD. The accurate analytical models of the tooth torsional deformation for calculating the specific positions along TWD are rarely founded and discussed in the existing modelling studies.

In the traditional TVMS analytical model of gears with ESC fault, the contact stiffness of the tooth pair is calculated by the linear Hertz contact theory. However, most studies have shown that the contact deformation and contact force between tooth pairs have a nonlinear relationship, and the contact stiffness is closely related to the contact force [32-34]. Hence, the NDL along TWD aroused by the ESC will inevitably change the contact characteristics along TWD of the tooth pairs with ESC and result in the deviation in TVMS excitation, while this influence is also not considered in the traditional models. In addition, the nonlinearity of the contact stiffness will lead to the coupling relationship between TVMS and load distribution, and thus the TVMS and load distribution need to be calculated in an iterative way [32-34]. However, the existing TVMS calculation models [32-34] based on the nonlinear Hertzian contact theory only pay attention to the iterative relationship between the TVMS and the load distribution of the meshing tooth pairs, but can not reveal the coupling relationship between the TVMS and the NDL along TWD caused by the asymmetric tooth errors or faults.

From the above review, the traditional TVMS analytical models of gear with ESC ignore the effects of tooth torsional deformation and the nonlinear contact characteristic changes caused by the NDL along TWD, and the analytical models of tooth torsional deformation and load distribution along TWD of the gears with ESC are seldom investigated and discussed. In addition, the iterative relationship between the TVMS and the load distribution between the meshing tooth pairs is well clarified by the existing TVMS calculation models based on the nonlinear Hertzian contact theory, but the iterative relationship between the TVMS and the load distribution along TWD is rarely studied and still unclear. Therefore, we will present our study in the following aspects of TVMS and load distribution modelling, which form the main contributions of the study:

(1) An analytical model of the tooth torsional deformation is proposed based on the slicing method. This model can calculate the tooth torsional deformation at any position along TWD of gears with asymmetric load distribution along TWD, which is not possible with the existing formulas in [31, 32] for calculating the tooth torsional deformation.

(2) Based on (1), a parallel slice stiffness model of the tooth pair with ESC is developed considering the tooth torsional deformation and the nonlinear contact characteristic changes as well as the slice coupling effect caused by the NDL along TWD. This model can express the coupling relationship between the stiffness and the load at each slice position along TWD, while the traditional models [13,14, 23-26] can not achieve this expression.

(3) Based on (2), a double-layer iterative calculation method for the TVMS and load distributions of the gear with ESC is proposed, in which the relationships between the slice stiffness and load along TWD as well as the TVMS and load distribution between the meshing tooth pairs are both considered. The proposed iterative calculation method can realize the accurate and fast decoupling calculation of the TVMS and the load distribution along the TWD, which cannot be done by the existing TVMS iterative calculation methods [32-34].

Based on the proposed two models in (1) and (2) and one method in (3), the double-layer iterative analytical model for calculating the TVMS and load distributions of the gear with ESC is finally formed. Based on the proposed double-layer iterative analytical model, the ESC parameters and applied torque on the torsional deformation, TVMS, and load distributions of the gear with ESC are investigated and discussed in this paper.

The rest of the paper is arranged as follows: The problem to be addressed in the paper is described in

Section 2. The proposed double-layer iterative analytical model of TVMS and load distributions of the gear with ESC is presented in Section 3. The FE models for verifying the proposed analytical model are introduced in Section 4. The calculated results based on the proposed models are analyzed and discussed in Section 5. In the end, some main conclusions are summarized in Section 6.

2. Problem formulation

To clearly present the problem to be solved in this paper, the schematic diagrams of the load distribution and its coupling relationship with TVMS of the gear with ESC fault are displayed in Fig. 2, where, Fig. 2 (a) shows the schematic diagram of the load distribution between the healthy tooth pair and the tooth pair with ESC fault, Fig. 2 (b) displays the schematic diagram of the load distribution along TWD of the tooth with ESC, and Fig. 2 (c) presents the coupling relationship between the TVMS and load distributions of the gear with ESC fault.
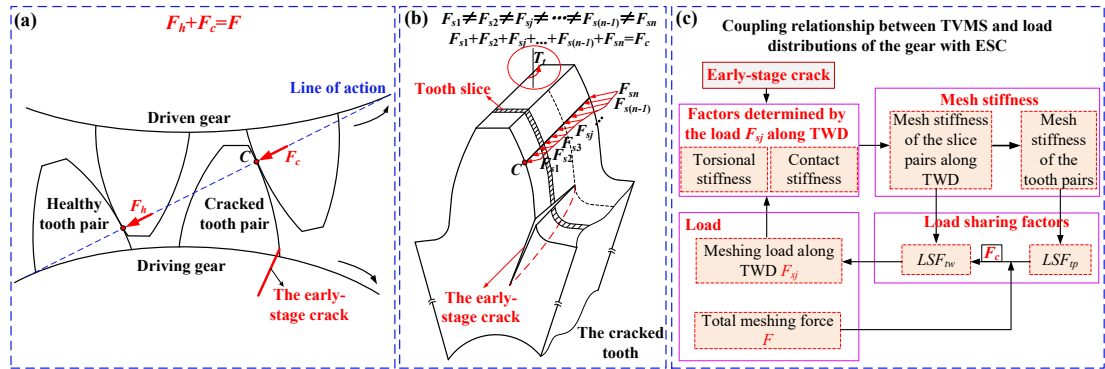
Fig. 2. Schematic diagram of load distribution and its coupling relationship with TVMS of gears with ESC fault: (a) load distribution between meshing tooth pairs, (b) load distribution along TWD, (c) coupling relationship between TVMS and load distributions.

In Fig. 2 (a), F_h and F_c separately represent the total mesh forces of the healthy and cracked tooth pairs, the cracked and healthy tooth pairs jointly bear the total meshing force F in the double-tooth meshing zones and their bearing capacities mainly depend on their mesh stiffness. It can be observed in Fig. 2 (b) that the ESC generally does not run through the whole tooth width, but distributes non-uniformly along the TWD, which will lead to uneven distribution of the tooth stiffness and load along TWD. The non-uniform distribution of the load F_{sj} along TWD will generate additional tooth torsional torque T_t and will force the gear tooth to twist and result in different tooth torsional deformation at each contact position along TWD. In addition, the contact stiffness of the tooth pair is closely related to the meshing force [32-34], thus the NDL F_{sj} along TWD will also lead to the uneven tooth contact deformations along TWD. The above two changes caused by the NDL along TWD will inevitably influence the TVMS of the tooth pair with ESC, while this influence is usually ignored in the traditional TVMS analytical models [13,14, 23-26] of gears with ESC, which is bound to cause the calculation error when using the traditional models. In addition, the analytical model that can calculate the tooth torsional deformation at each slice position along TWD is rarely found in the existing studies and need to be further developed.

As presented in Fig. 2 (c), the tooth torsional stiffness and contact stiffness of the tooth pairs with ESC are both related to the load F_{sj} along TWD and in turn, they also affect the load distribution along TWD. Thus there is a coupling relationship between the TVMS and the NDL along TWD in the gears with ESC, and its TVMS and load distributions need to be decoupled iteratively. While the existing

TVMS and load distribution calculation models [32-34] based on the nonlinear Hertzian contact theory only pay attention to the iterative relationship between the TVMS and the load distribution between the meshing tooth pairs, but can not reflect the coupling relationship between the TVMS and the NDL along TWD. Thus, in the TVMS and load distribution modelling of the gear with ESC, the coupling relationships between the slice stiffness and load distribution along TWD (inner-layer iteration) as well as the TVMS and load distribution between the meshing tooth pairs (outer-layer iteration) should both be considered.

Therefore, the objective of this study is to establish a double-layer iterative analytical model of TVMS and load distributions of the gear with ESC fault considering the effects of NDL along TWD. Then to clarify the coupling relationship between TVMS and load distributions along TWD and study the influence of the ESC parameters and applied load on the tooth torsional deformation, load distributions, and TVMS excitation of the gears with ESC fault.

3. Proposed double-layer iterative analytical model for TVMS and load distributions of gear with ESC fault

As displayed in Fig. 2 (b), the tooth pair with ESC has different load distribution characteristics along TWD compared to the healthy tooth pair, causing its TVMS calculation modelling is also different from the healthy one. Therefore, the TVMS analytical modelling of the tooth pairs with ESC is firstly carried out in Section 3.1, in which the tooth torsional deformation model and the parallel slice stiffness model of the tooth pair with ESC are separately developed and presented; Then, the TVMS analytical models of the healthy tooth pair is also briefly presented in Section 3.2; On this basis, the TVMS and load distribution expressions of gears with ESC is finally developed in Section 3.3. In the end, the proposed double-layer iterative method is described in Section 3.4.

## 3.1 TVMS modelling of tooth pair with ESC using the slicing method

Establishing the analytical TVMS model of the tooth pair with ESC fault is a key content for the proposed double-layer iterative model, which can help us understand the coupling relationship between the stiffness and load along TWD of the tooth pair with ESC. Therefore, the TVMS modelling of the tooth pair with ESC fault is carried out in this section.

3.1.1 Proposed parallel slice stiffness model of tooth pair with ESC

The physical model of the tooth pair with the ESC based on the slicing method is presented in Fig. 3. As Fig. 3 shows, this paper assumes that the crack is distributed as a parabolic shape along TWD, the maximum depth value of the crack is q_0, and the maximum distribution length of the crack along the TWD is W_c. In Fig. 3 (d), the relationship between the crack depth $q(z)$ and the tooth direction position z_j of the cracked slice can be expressed as,

$$q(z) = q_0 \sqrt{\frac{W_c - z_j - W/2}{W_c}} \tag{1}$$

Here, q_0 denotes the maximum depth of ESC, W_c means the length of the ESC, W is the tooth width.
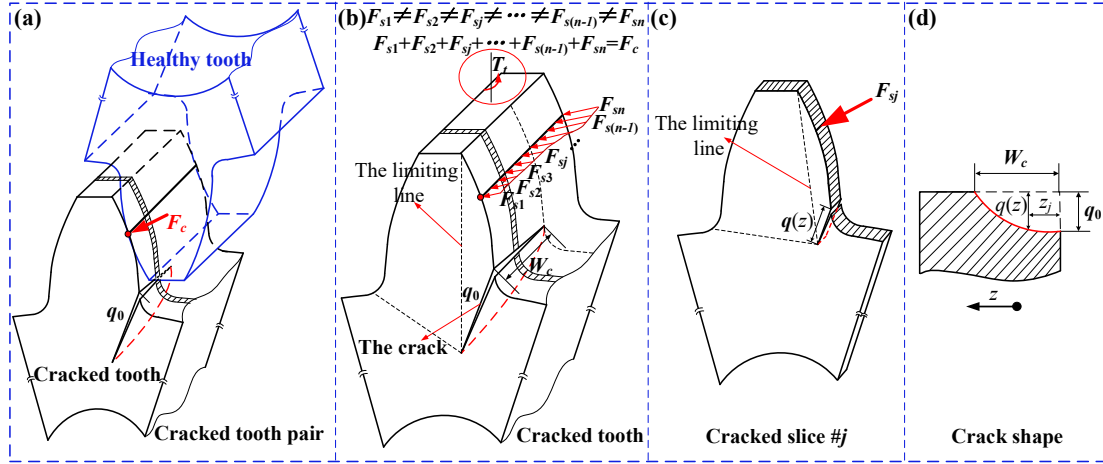
Fig. 3. Diagram of tooth pair with ESC fault: (a) cracked tooth pair in meshing, (b) load distribution of cracked tooth, (c) cracked slice, (d) crack shape.

To establish the coupling relationship between the slice stiffness and the load distribution along TWD, a parallel slice stiffness model of the tooth with ESC is developed and shown in Fig. 4, which is mainly divided into two kinds of slices: the cracked slices and the healthy slices. Different from the tooth in the healthy tooth pair, the load F_{sj} along TWD of the tooth with ESC would lead to additional torsional deformation. Therefore, to represent the torsional deformation of each slice under the action of load F_{sj}, the torsional stiffness is added to the proposed parallel slice stiffness of the tooth with ESC, which is represented by k_{ctj} or k_{htj} in Fig. 4. In addition, due to the uniform distribution of stiffness and load along TWD, the deformations of the tooth slices along TWD are not equal to each other, which will cause the coupling force between the adjacent tooth slices [28, 35]. While the slice coupling effect is usually ignored in the traditional models [13,14, 23-26]. Therefore, in the proposed parallel slice stiffness model, the slice coupling stiffness is also added to simulate the coupling effects between slices, which is represented by the red spring $k_{cp(j-1)j}$ in Fig. 4.
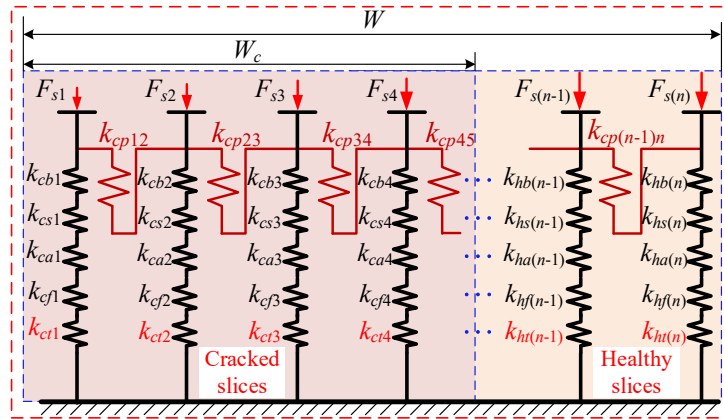
Fig. 4. Parallel slice stiffness model of the tooth with ESC.

The proposed parallel slice stiffness model of the single tooth pair with ESC before and after deformation is presented in Fig. 5, in which the total deformation of the cracked tooth pair is presented with the symbol δ. In this model, the deformations of each slice of the tooth pair with ESC and the contact deformation between meshing slice pairs are not equal due to the non-uniformity of sliced tooth stiffness and load distribution as well as the coupling effect between tooth slices. From Fig. 5 we can see that the slice-type compositions of the cracked and healthy teeth of the tooth pair with ESC are different, that is,

the healthy tooth is all composed of healthy slices, while the cracked tooth consists of two kinds of slices: the cracked slices and the healthy slices. Hence, the slice stiffness expressions of the cracked and healthy tooth in the tooth pair with ESC is different from each other and need to be respectively derived out.

The establishment process of the analytical TVMS expression for the proposed parallel slice stiffness model of the single tooth pair with ESC is given in the following sections, where, the modelling of the slice torsional deformation of the cracked and healthy teeth is firstly conducted in Section 3.1.2. On this basis, the slice stiffness expressions of the cracked and healthy teeth of the tooth pair with ESC are derived separately in Sections 3.1.3 and 3.1.4. Finally, the analytical TVMS expression for the proposed parallel slice stiffness model of the single tooth pair with ESC is developed and presented in Section 3.1.5.
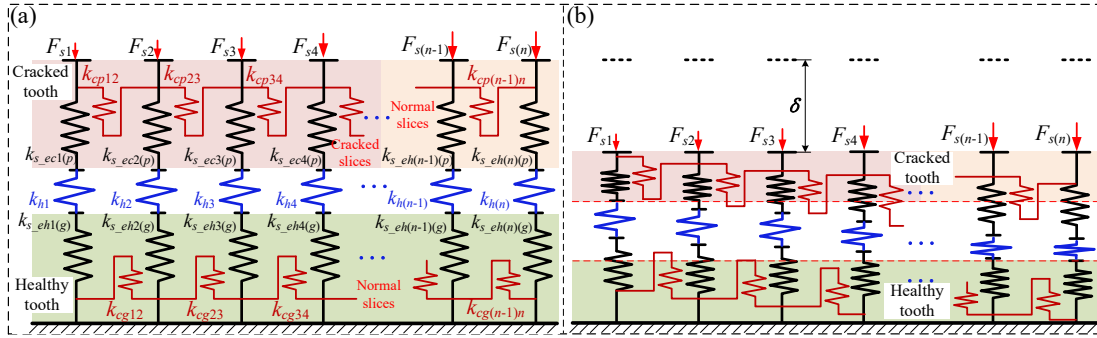

Fig. 5. Proposed parallel slice stiffness model of tooth pair with ESC: (a) before deformation, (b) after deformation.

3.1.2 Analytical model of tooth torsional deformation

From Section 3.1.1 we can know that obtaining the tooth torsional stiffness of each slice along TWD is the first prerequisite for establishing the analytical TVMS expression of the proposed parallel slice stiffness model. Since the existing formulas in [31, 32] for the tooth torsional deformation can not obtain the actual tooth torsional deformation of specific positions along TWD and are unable to be used directly in the proposed parallel slice stiffness model, a new analytical model of the tooth torsional deformation is developed in this section.

The physical models for calculating the slice torsional deformation of the tooth with ESC are displayed in Fig. 6. As Fig. 6 (a) shows, due to the existence of the crack, the effective deformation zone of the cracked tooth will change. Scholars usually use the limiting line to calibrate the effective deformation zone of cracked teeth, that is, the tooth dead zone shown in Fig. 6 (a) does not participate in the deformation [31], only the shaded Zones I, II and III will be deformed. A-A and B-B refer to the cross sections at the tooth profile position x_i and the meshing point, respectively. F_c is the meshing force of the cracked tooth, and F_a and F_b denote the axial compression and shear forces decomposed by meshing force F_c. Fig. 6 (b) shows the torsional deformation diagram of cross-section B-B. In Fig. 6 (b), rectangle $ABCD$ denotes the actual cross-section B-B of the cracked tooth, and the parabola DEF represents the dead zone of cross-section B-B considering the influence of the ESC, and its maximum height is h_{qxi}. points O_0 and O_2 represent the centroid of the rectangle $ABCD$ and the parabola DEF, respectively. The coordinate system $Y_0O_0Z_0$ refers to a rectangular coordinate system established with O_0 as the origin. Therefore, the actual deformation region of cross-section B-B is the shape $ABCEF$ and its centroid is O_1. The deviation distance of O_1 from the Y_0-axis and Z_0-axis of the original coordinate $Y_0O_0Z_0$ is Δz and Δy, respectively. The shaded part represents the jth slice, and its width is ΔW. z_j denotes the Z_0-axis coordinate position of the jth slice in the coordinate system. A row of arrows means the NDL

along TWD of the cracked tooth pair, in which the red arrow denotes the shear force F_{bj} exerted on the jth slice. δ_{tcj} represents the torsional deformation of the jth slice of the cracked tooth.

Ignoring the bending, compression and other tooth deformations, cross-section B-B will produce an overall tooth torsional deformation around the center O_1 under the action of torsional moment $T_{t(c)}$ caused by the NDL along TWD, and the corresponding torsional angle is φ_c. cross-section B-B after torsion is displayed with the green rectangle $A'B'C'D'$. It can be seen that the direction of torsional deformation of slices on both sides of centroid O_1 is opposite, which is determined by the actual torsional angle φ_c. Consistent with other tooth deformations, the proposed model also assumes that the torsional deformations in the same direction as the load direction are positive, and those in the opposite direction are negative. Therefore, the torsional stiffness k_{ctj} and k_{htj} shown in Fig. 4 also have positive and negative values, where the positive value indicates that the torsional stiffness of the jth slice under the action of shear force F_{bj} will increase the total tooth deformation, while the negative value is the opposite.
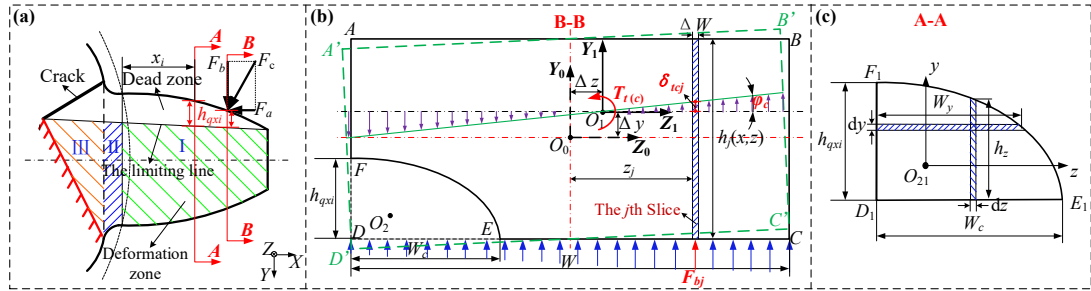
Fig. 6. Physical models for calculating slice torsional stiffness of the tooth with ESC: (a) deformation zone of the cracked tooth, (b) torsional deformation diagram of cross-section B-B, (c) parameters of dead zone $D_1E_1F_1$.

According to the definition of torsional deformation, the tooth torsional deformation angle φ_c under the action of torsional moment $T_{t(c)}$ can be expressed as,

$$\varphi_c = \int_0^d \frac{T_{t(c)}}{GI_{px(c)}}dx = \int_0^d \frac{F_b Z_F}{GI_{px(c)}}dx = \int_0^d \frac{\sum\limits_{j=1}^{n} F_{bj} \cdot \left[z_j - \Delta z_F\right]}{GI_{px(c)}}dx$$

$$= \int_0^{d_1} \frac{\sum\limits_{j=1}^{n} F_{sj}\left[z_j - \Delta z_F\right]\cos\alpha_1}{GI_{px1(c)}}dx_1 + \int_0^{d_2} \frac{\sum\limits_{j=1}^{n} F_{sj}\left[z_j - \Delta z_F\right]\cos\alpha_1}{GI_{px2(c)}}dx_2 + \int_0^{d_3} \frac{\sum\limits_{j=1}^{n} F_{sj}\left[z_j - \Delta z_F\right]\cos(\alpha_1 + \theta)}{GI_{px3(c)}}dx_3$$

$$(2)$$

where $I_{px(c)}$ denotes the polar moment of inertia of the cracked tooth and is a function of the tooth profile position x_i. Z_F and Δz_F respectively represent the equivalent moment arm of the tooth load around the section center O_1 and the offset of the center O_1 along the Z_0-axis in the cross-section B-B.

Then the torsional deformation of the jth slice can be deduced as,

$$\delta_{tcj} = (z_j - \Delta z_F) \cdot \tan\varphi_c \tag{3}$$

where the position z_j is a function of the slice number j and can be defined as,

$$z_j = \frac{(2j-1)\Delta W - W}{2}, j = 1, 2, \cdots n \tag{4}$$

The equivalent torsional stiffness of the jth slice of the cracked tooth can be finally calculated as,

$$k_{tcj} = \frac{F_{sj}}{\delta_{tcj}} = \frac{F_{sj}}{(z_j - \Delta z_F)\tan\varphi_c} \tag{5}$$

The polar moment of inertia $I_{px(c)}$ in Eq. (2) is derived as follows:

The offset distance $\Delta z(x_i)$ and $\Delta y(x_i)$ of the centroid O_1 of cross-section B-B at the tooth profile position x_i relative to the Y_0 and Z_0 axes can be respectively expressed as,

$$\Delta z(x_i) = \frac{\frac{2}{3}W_c h_{qxi}\left(\frac{1}{2}W - \frac{2}{5}W_c\right)}{W \cdot h_{hxi} - \frac{2}{3}W_c h_{qxi}}, i = 1,2,3 \tag{6}$$

$$\Delta y(x_i) = \frac{\frac{2}{3}W_c h_{qxi}\left(\frac{1}{2}h_{hxi} - \frac{3}{8}h_{qxi}\right)}{W \cdot h_{hxi} - \frac{2}{3}W_c h_{qxi}}, i = 1,2,3 \tag{7}$$

Here, the effective height of the tooth cantilever beam in Zone *III* can be deduced as,

$$h_{hx3} = \frac{d_3(\cot\gamma + \tan\nu)}{(\sin\theta\tan\nu + \cos\theta)} \tag{8}$$

Fig. 6 (c) shows the calculation parameters of the moment of inertia in the parabolic dead zone of section A-A. By comparing with Fig. 6 (b), it can be seen that the dead zone *DEF* changes to $D_1E_1F_1$ when the section position changed from cross-section B-B to section A-A, and its centroid changes from O_2 to O_{21}. The rectangular coordinate system $zO_{21}y$ is established using the parabolic center O_{21} as the origin, and the shaded sections dy and dz respectively represent the micro-segments of the dead zone $D_1E_1F_1$ along the y and z axis in the rectangular coordinate system $zO_{21}y$. Then the height h_z corresponding to the micro-segment dz can be expressed as,

$$h_z = h_{qxi}\sqrt{\frac{3}{5} - \frac{z}{W_c}}, i = 1,2,3 \tag{9}$$

where z is the coordinate of micro-segment dz on the z-axis in the coordinate system $zO_{21}y$. The maximum height of the parabola h_{qxi} can be calculated as $h_{qxi} = h_{hxi} - h_{cxi}$.

The moment of inertia of the parabolic dead zone $D_1E_1F_1$ related to its z-axis can be derived as,

$$I_{py} = \int_{-\frac{2}{5}W_c}^{\frac{3}{5}W_c} z^2 h_z d_z = \int_{-\frac{2}{5}W_c}^{\frac{3}{5}W_c} z^2 h_{qxi}\sqrt{\frac{3}{5} - \frac{z}{W_c}} d_z = \frac{8W_c^3 \cdot h_{qxi}}{175} \tag{10}$$

The moment of inertia of the parabolic dead zone $D_1E_1F_1$ relative to the Z_1-axis in the coordinate system $Y_1O_1Z_1$ can be given as,

$$I_{y,p} = I_{pz} + \frac{2}{3}h_{qxi}W_c\left[\Delta z(x_i) + \frac{W}{2} - \frac{2}{5}W_c\right]^2 \tag{11}$$

Similarly, the width W_y corresponding to the micro-segment dy in the coordinate system $zO_{21}y$ can be written as,

$$W_y = W_c\sqrt{\frac{5}{8} - \frac{y}{h_{qxi}}} \tag{12}$$

The moment of inertia of the dead zone $D_1E_1F_1$ related to its y-axis can be deduced as,

$$I_{pz} = \int_{-\frac{3}{8}h_{qxi}}^{\frac{5}{8}h_{qxi}} y^2 W_y d_y = \int_{-\frac{3}{8}h_{qxi}}^{\frac{5}{8}h_{qxi}} y^2 W_c\sqrt{\frac{5}{8} - \frac{y}{h_{qxi}}} d_y = \frac{31W_c \cdot h_{qxi}^3}{672} \tag{13}$$

The moment of inertia of dead zone $D_1E_1F_1$ related to the Y_1-axis can be calculated as,

$$I_{z,p} = I_{py} + \frac{2}{3} h_{qxi} W_c \left(\Delta y + \frac{h_{hxi}}{2} - \frac{3}{8} h_{qxi} \right)^2 \tag{14}$$

The moment of inertia of rectangle $ABCD$ relative to axis Y_1 and axis Z_1 in coordinate system $Y_1 O_1 Z_1$ can be derived as,

$$I_{y,r} = \frac{1}{12} h_{hxi} W^3 + h_{hxi} W \left[\Delta z(x_i) \right]^2, i = 1,2,3 \tag{15}$$

$$I_{z,r} = \frac{1}{12} h_{hxi}{}^3 W + h_{hxi} W \left[\Delta y(x_i) \right]^2, i = 1,2,3 \tag{16}$$

Combined with the above equations, the polar moment of inertia of each effective deformed section $ABCEF$ relative to the centroid O_1 in Zones I, II and III of the cracked tooth can be finally expressed as,

$$I_{pxi(c)} = I_{z,r} + I_{y,r} - I_{z,p} - I_{y,p}, i = 1,2,3 \tag{17}$$

The healthy tooth meshing with the tooth with ESC will also produce torsional deformation due to the uneven load distribution. Fig. 7 displays the physical models for calculating the slice torsional stiffness of the healthy tooth, where δ_{thj} represents the torsional deformation of the jth slice of the healthy tooth, $T_{t(h)}$ and φ_h denote the torsional moment and torsional angle of the healthy tooth, respectively. Different from the tooth with ESC shown in Fig. 6, the effective deformation zone of the healthy tooth is only Zones I and II, as Fig. 7 (a) shows. Without the effects of ESC, the centroid of the stressed tooth section will be the center point O_3 of the rectangle $ABCD$ presented in Fig. 7 (b). Therefore, the torsional deformation angle of the healthy tooth can be calculated as,

$$\varphi_h = \int_0^{d_1} \frac{\sum_{j=1}^{n} F_{sj} z_j \cos\alpha_1}{GI_{px_1(h)}} dx_1 + \int_0^{d_2} \frac{\sum_{j=1}^{n} F_{sj} z_j \cos\alpha_1}{GI_{px_2(h)}} dx_2 \tag{18}$$

where the polar moment of inertia $I_{pxi(h)}$ of the healthy tooth relative to the centroid O_3 can be computed as,

$$I_{pxi(h)} = \frac{1}{12} h_{hxi} W^3 + \frac{1}{12} h_{hxi}{}^3 W, i = 1,2 \tag{19}$$
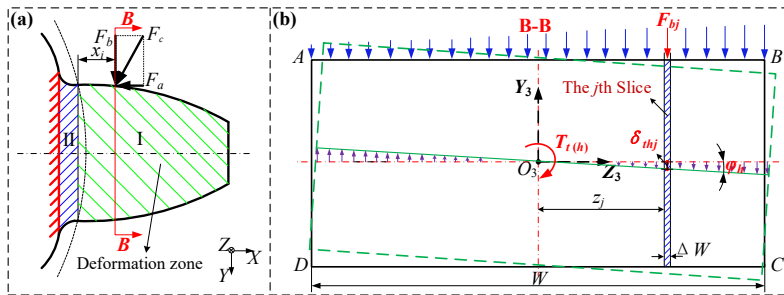

Fig. 7. Physical models for calculating slice torsional stiffness of the healthy tooth: (a) deformation zone of healthy tooth, (b) torsional deformation diagram of cross-section B-B.

Then the equivalent torsional stiffness of the jth slice of the healthy tooth can finally be deduced as,

$$k_{thj} = \frac{F_{sj}}{\delta_{thj}} = \frac{F_{sj}}{z_j \tan\varphi_h} \tag{20}$$

In Eq. (20), the positive and negative values of the torsional stiffness k_{thj} of the healthy tooth also depend on the torsional angle φ_h, which is the same as the definition of the tooth with ESC.

3.1.3 Stiffness analytical expression of the slices of the healthy tooth

The physical tooth model of the cantilever beam for calculating the stiffness of the slice in the healthy tooth is shown in Fig. 8. The model assumes the gear tooth as a variable section cantilever beam fixed on the dedendum circle, which can be divided into two parts: Zone I and Zone II. In Fig. 8, F_{sj} is the meshing force of the tooth slice, F_{aj} and F_{bj} are the axial compression and shear forces decomposed by F_{sj}. Other symbols in Fig. 8 can be found in the Nomenclature of this paper. In this section, the energy method [12, 36] is adopted to calculate the stiffness of slices of the healthy tooth.
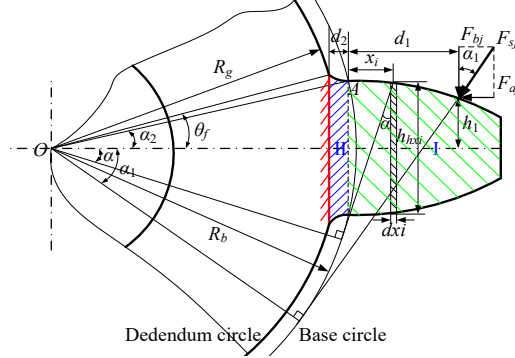

Fig. 8. Physical model of the cantilever beam of healthy slice.

Under the action of slice meshing force F_{sj}, the bending deformation energy U_{bhj}, axial compression deformation energy U_{ahj} and shear deformation energy U_{shj} stored in Zone I and Zone II of the jth sliced healthy tooth can be respectively expressed as [12, 36],

$$
\begin{cases}
U_{bhj} = \dfrac{F_{sj}^2}{2k_{bhj}} = \displaystyle\int_0^{d_1} \dfrac{\left[F_{bj}\cdot(d_1 - x_1) - F_{aj}\cdot h_1\right]^2}{2EI_{hx_1}}dx_1 + \int_0^{d_2} \dfrac{\left[F_{bj}\cdot(d_1 + x_2) - F_{aj}\cdot h_1\right]^2}{2EI_{hx_2}}dx_2 \\[4mm]
U_{ahj} = \dfrac{F_{sj}^2}{2k_{ahj}} = \displaystyle\int_0^{d_1} \dfrac{F_{aj}^2}{2EA_{hx_1}}dx_1 + \int_0^{d_2} \dfrac{F_{aj}^2}{2EA_{hx_2}}dx_2 \\[4mm]
U_{shj} = \dfrac{F_{sj}^2}{2k_{shj}} = \displaystyle\int_0^{d_1} \dfrac{1.2F_{bj}^2}{2GA_{hx1}}dx_1 + \int_0^{d_2} \dfrac{1.2F_{bj}^2}{2GA_{hx_2}}dx_2
\end{cases}
\tag{21}
$$

of which,

$$
F_{bj} = F_{sj}\cos\alpha_1 , \; F_{aj} = F_{sj}\sin\alpha_1
\tag{22}
$$

By deducing Eq. (21), the stiffness expression of the bending k_{bhj}, axial compression k_{ahj} and shear k_{shj} of the sliced healthy tooth can be obtained as,

$$
\begin{cases}
\dfrac{1}{k_{bhj}} = \displaystyle\int_0^{d_1} \dfrac{\left[(d_1 - x_1)\cos\alpha_1 - h_1\sin\alpha_1\right]^2}{EI_{hx1}}dx_1 + \int_0^{d_2} \dfrac{\left[(d_1 + x_2)\cos\alpha_1 - h_1\sin\alpha_1\right]^2}{EI_{hx2}}dx_2 \\[4mm]
\dfrac{1}{k_{ahj}} = \displaystyle\int_0^{d_1} \dfrac{\sin^2\alpha_1}{EA_{hx1}}dx_1 + \int_0^{d_2} \dfrac{\sin^2\alpha_1}{EA_{hx2}}dx_2 \\[4mm]
\dfrac{1}{k_{shj}} = \displaystyle\int_0^{d_1} \dfrac{1.2\cos^2\alpha_1}{GA_{hx1}}dx_1 + \int_0^{d_2} \dfrac{1.2\cos^2\alpha_1}{GA_{hx2}}dx_2
\end{cases}
\tag{23}
$$

The specific expressions of parameters in the above formulas can be found in Appendix A.

The fillet foundation of the gear tooth will also deform under the action of meshing force, and the fillet foundation k_{fhj} of the jth sliced healthy tooth can be calculated as [37],

$$\frac{1}{k_{fhj}} = \frac{\cos^2 \alpha_1}{E \Delta W}\left[L^*\left(\frac{\mu_f}{S_f}\right)^2 + M^*\left(\frac{\mu_f}{S_f}\right) + P^*\left(1 + Q^* \tan^2 \alpha_1\right)\right] \qquad (24)$$

Therefore, considering the effects of the slice torsional deformation, the total stiffness k_{t_ehj} of the jth slice of the healthy tooth can be calculated as,

$$\frac{1}{k_{t\_ehj}} = \frac{1}{k_{bhj}} + \frac{1}{k_{shj}} + \frac{1}{k_{ahj}} + \frac{1}{k_{fhj}} + \frac{1}{k_{thj}[F_{sj}]} \qquad (25)$$

where the symbol $[F_{sj}]$ is used to emphasize that the slice torsional stiffness is related to the slice load F_{sj}.

3.1.4 Stiffness analytical expression of the slices of the tooth with ESC

Fig. 9 shows the physical model of the cantilever beam of the sliced tooth with ESC, where Fig. 9 (a) and (b) display the calculation parameters of the tooth and body deformation zones respectively. In Refs. [8, 9], there are various crack propagation paths, and the crack propagation direction and initial position are also different. To reflect the universality of the model presented in this paper, Fig. 9 shows the special situation that the crack propagates into the gear body and its initial position is on the gear body, while the other crack path situations, such as tooth cracks, are also included in this model, which can be referred to Refs. [6, 7, 38].

In Fig. 9 (a) and (b), AQ represents the crack of the slice tooth; v denotes the crack angle; $q(z)$ is the crack depth shown in Fig. 3 (d), which is related to the slice position z_j along TWD. BQ refers to the attachment position of the cantilever beam of the cracked slice. For the explanations and expressions of other symbols in Fig. 9 can be specifically seen in Refs. [21, 22], which will not be repeated here.
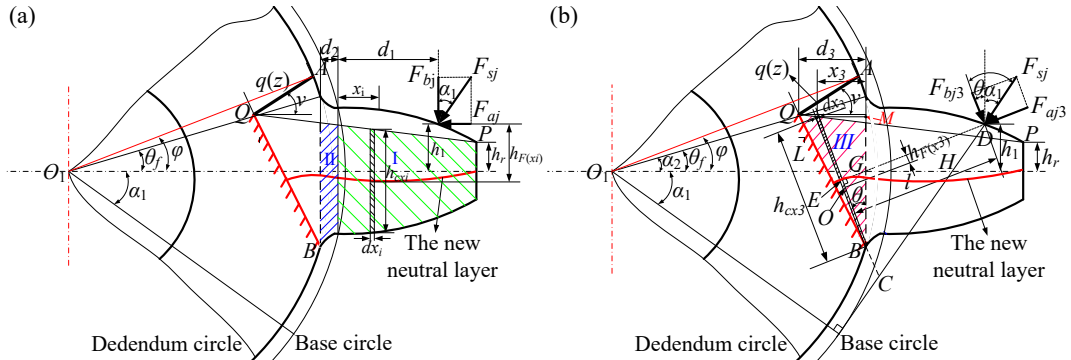

Fig. 9. Physical model of the cantilever beam of cracked slice: (a) tooth deformation zone [21], (b) body deformation zone [22].

As Fig. 9 shows, the shaded parts represent the effective deformation region of Zones I and II in the tooth area and Zone III in the body area, respectively. The previous TVMS analytical models [15, 17] of cracked gear believe that the crack can only change the effective tooth thickness of Zones I and II and the attachment area of the tooth beam on the gear body, which has a weakening effect on the gear TVMS. However, Yang et al. [21, 22] proposed that the crack would change the attachment position of the tooth cantilever beam, which not only resulted in the reduction of the effective tooth thickness but also lengthened and tilted the tooth beam. In other words, the deformation of Zone III in Fig. 9 (b) should also be taken into account in the total tooth deformation. In addition, the crack will be opening under the action of meshing force, which will cause the change in the central layer of the effective tooth deformation zone, leading to the different calculation methods of the bending and compression stiffness from the traditional model [39]. Therefore, the influence of the crack opening state and the change of

tooth attachment position caused by the crack are both considered in this modelling.

According to the VADEI method proposed in [22], the force decomposition is different when calculating the stiffness in different tooth beam zones, which can be expressed as,

$$F_{bj} = \begin{cases} F_{sj}\cos\alpha_1, & i = 1,2 \\ F_{sj}\cos(\alpha_1 + \theta), & i = 3 \end{cases} \tag{26}$$

Therefore, the tooth stiffness of the jth slice can be further written as,

$$\begin{cases} \dfrac{1}{k_{bcj}} = \int_0^{d_1} \dfrac{\left[(d_1 - x_1)\cos\alpha_1 - h_{F(x_1)}\sin\alpha_1\right]^2}{EI_{cx1}}dx_1 + \int_0^{d_2} \dfrac{\left[(d_1 + x_2)\cos\alpha_1 - h_{F(x_2)}\sin\alpha_1\right]^2}{EI_{cx2}}dx_2 \\ \quad + \int_0^{d_3} \dfrac{\left[l\cos(\alpha_1 + \theta) - h_{F(x_3)}\sin(\alpha_1 + \theta)\right]^2}{EI_{cx3}}dx_3 \\ \dfrac{1}{k_{acj}} = \int_0^{d_1} \dfrac{\sin^2\alpha_1}{EA_{cx1}}dx_1 + \int_0^{d_2} \dfrac{\sin^2\alpha_1}{EA_{cx2}}dx_2 + \int_0^{d_3} \dfrac{\sin^2(\alpha_1 + \theta)}{EA_{cx3}}dx_3 \\ \dfrac{1}{k_{scj}} = \int_0^{d_1} \dfrac{1.2\cos^2\alpha_1}{GA_{cx1}}dx_1 + \int_0^{d_2} \dfrac{1.2\cos^2\alpha_1}{GA_{cx2}}dx_2 + \int_0^{d_3} \dfrac{1.2\cos^2(\alpha_1 + \theta)}{GA_{cx3}}dx_3 \end{cases} \tag{27}$$

For the calculation of the fillet foundation stiffness of cracked teeth, Chen [11] and Yang [21] proposed two analytical models. Chen's model would produce a large error in the body crack case, while Yang's model could satisfy the calculation accuracy for both the tooth and body cracked teeth. Therefore, the calculation formula of fillet foundation stiffness in [21] is adopted in this modelling,

$$\frac{1}{k_{fcj}} = \frac{\cos^2(\alpha_1 + \gamma)}{E\Delta W}\left[L^*\left(\frac{\mu_f'}{S_f'}\right)^2 + M^*\left(\frac{\mu_f'}{S_f'}\right) + P^*\left(1 + Q^*\tan^2(\alpha_1 + \gamma)\right)\right] \tag{28}$$

The analytical expressions of parameters s_f' and u_f' in Eq. (28) can be seen in Appendix B, and other parameters can be found in Ref. [37].

As the tooth with ESC includes healthy and cracked slices, the total stiffness k_{t_ecj} of the jth slice in the tooth with ESC can be finally deduced as,

$$\frac{1}{k_{t\_ecj}} = \begin{cases} \dfrac{1}{k_{bhj}} + \dfrac{1}{k_{shj}} + \dfrac{1}{k_{ahj}} + \dfrac{1}{k_{fhj}} + \dfrac{1}{k_{thj}[F_{sj}]}, & \text{if } z_j \in [W_c - W/2,\ W/2] \\ \dfrac{1}{k_{bcj}} + \dfrac{1}{k_{scj}} + \dfrac{1}{k_{acj}} + \dfrac{1}{k_{fcj}} + \dfrac{1}{k_{tcj}[F_{sj}]}, & \text{if } z_j \in [-W/2,\ W_c - W/2] \end{cases} \tag{29}$$

3.1.5 TVMS and load distribution expressions of tooth pair with ESC considering slice coupling effect

As shown in Fig. 4, the coupling stiffness $k_{cj(j+1)}$ is adopted in the proposed parallel slice stiffness model to simulate the coupling effect between slices. The calculation of the coupling stiffness can be defined as [28],

$$k_{cj(j+1)} = C_c \frac{k_{tj} + k_{t(j+1)}}{2}\left(\frac{m}{\Delta W}\right)^2 \tag{30}$$

of which, k_{tj} and $k_{t(j+1)}$ respectively represent the total stiffness of two adjacent slices. m refers to the gear modulus, and C_c denotes the slice coupling coefficient.

The slice stiffness model established in Ref. [28] only considers the tooth part, not including the gear body part, while the model proposed in this paper includes both the tooth and body parts. Hence, the coupling stiffness between slices should be significantly greater than the value in [28]. Therefore, $C_c=750$

is adopted in this study.

Considering the slice coupling effect, the load on the slices along TWD can be expressed as [28, 35],

$$
\begin{cases}
k_{t1}\delta_{t1} + k_{c12}\left(\delta_{t1} - \delta_{t2}\right) = F_{s1} \\
-k_{c12}\left(\delta_{t1} - \delta_{t2}\right) + k_{t2}\delta_{t2} + k_{c23}\left(\delta_{t2} - \delta_{t3}\right) = F_{s2} \\
-k_{c23}\left(\delta_{t2} - \delta_{t3}\right) + k_{t3}\delta_{t3} + k_{c34}\left(\delta_{t3} - \delta_{t4}\right) = F_{s3} \\
\vdots \\
-k_{c(n-2)(n-1)}\left(\delta_{t(n-2)} - \delta_{t(n-1)}\right) + k_{t(n-1)}\delta_{t(n-1)} + k_{c(n-1)n}\left(\delta_{t(n-1)} - \delta_{tn}\right) = F_{s(n-1)} \\
-k_{c(n-1)n}\left(\delta_{t(n-1)} - \delta_{tn}\right) + k_{tn}\delta_{tn} = F_{sn}
\end{cases}
\tag{31}
$$

Transform Eq. (31) into matrix form, we can get,

$$
\mathbf{K_C}\boldsymbol{\delta_t} =
\begin{bmatrix}
k_{t1}+k_{c12} & -k_{c12} & 0 & 0 & 0 & 0 \\
& k_{t2}+k_{c12}+k_{c23} & -k_{c23} & 0 & 0 & 0 \\
& & k_{t3}+k_{c23}+k_{c34} & -k_{c34} & 0 & 0 \\
& & & \ddots & \vdots & \vdots \\
& \text{symmetric} & & & k_{t(n-1)}+k_{c(n-2)(n-1)}+k_{c(n-1)n} & -k_{c(n-1)n} \\
& & & & & k_{tn}+k_{c(n-1)n}
\end{bmatrix}
\begin{bmatrix}
\delta_{t1} \\ \delta_{t2} \\ \vdots \\ \vdots \\ \delta_{t(n-1)} \\ \delta_{tn}
\end{bmatrix}
=
\begin{bmatrix}
F_{s1} \\ F_{s2} \\ \vdots \\ \vdots \\ F_{s(n-1)} \\ F_{sn}
\end{bmatrix}
= \mathbf{F_s}
$$

$$\tag{32}$$

where $\mathbf{K_C}$ represents the slice stiffness matrix, $\boldsymbol{\delta_t}$ means the total deformation vector of the slices, and $\mathbf{F_s}$ refers to the meshing force vector of the slices. δ_{tj} is the deformation of the jth slice, and k_{tj} denotes the stiffness of jth slice of the healthy or cracked tooth, which can be expressed as,

$$
k_{tj} =
\begin{cases}
k_{t\_ehj}, & \text{if the tooth is healthy} \\
k_{t\_ecj}, & \text{if the tooth is cracked}
\end{cases}
\tag{33}
$$

Here, k_{t_ehj} and k_{t_ecj} can be calculated by Eqs. (25) and (29) respectively. It can be found that k_{tj} is coupled with the force F_{sj}, and its value is closely related to the magnitude of the force F_{sj}.

Then the total TVMS vector $\mathbf{K_{tp}}$ of the sliced tooth pairs along TWD can be obtained,

$$
\mathbf{K_{tp}} = \sum \left[\mathbf{K_{CP}}^{-1} + \mathbf{K_{CH}}^{-1} + \mathbf{K_{CG}}^{-1}\right]^{-1} = \left[K_{tp1},\, K_{tp2},\, \cdots,\, K_{tp(n-1)},\, K_{tpn}\right]
\tag{34}
$$

where $\mathbf{K_{CP}}$ and $\mathbf{K_{CG}}$ respectively denote the slice stiffness matrix of cracked and healthy teeth considering the slice coupling effect, which can be obtained through Eq. (32). K_{tpj} means the mesh stiffness of the jth slice pair of the tooth pair with ESC. $\mathbf{K_{CH}}$ denotes the contact stiffness matrix of sliced tooth pairs, which can be deduced as,

$$
\mathbf{K_{CH}} = diag\left(k_{h1}\,[F_{s1}], k_{h2}\,[F_{s2}], \cdots, k_{h(n-1)}\,[F_{s(n-1)}], k_{hn}\,[F_{sn}]\right)
\tag{35}
$$

In Eq. (35), k_{hj} represents the nonlinear Hertz contact stiffness of the jth tooth pair, and the symbol $[F_{sj}]$ is used to emphasize that the contact stiffness is related to the load F_{sj}. The expression of nonlinear Hertz contact stiffness of the jth meshing slice pair can be calculated as [40],

$$
k_{hj}[F_{sj}] = \frac{E^{0.9}\Delta W^{0.8}F_{sj}^{\,0.1}}{1.275}
\tag{36}
$$

The total TVMS $K_{ec\text{-}single}$ of the single tooth pair with ESC considering the slice coupling effect can be finally obtained as,

$$
K_{ec\_single} = \sum \mathbf{K_{tp}}
\tag{37}
$$

The load sharing factor LSF_{twj} of the jth slice pair can be finally given out,

$$LSF_{twj} = K_{tpj} / K_{ec\_single} \tag{38}$$

And the load of the jth meshing slice pair can be expressed as,

$$F_{sj} = F_c \cdot LSF_{twj} \tag{39}$$

3.2 TVMS modelling of the healthy tooth pair using the slicing method

The TVMS analytical model of healthy tooth pairs based on the slicing method is consistent with the traditional models because the load along TWD is uniformly distributed in the healthy tooth pairs. However, to highlight the difference of TVMS analytical models of the tooth pairs with ESC under the influence of NDL along TWD as well as to facilitate the later description of the iterative relationship of the load and TVMS between the healthy and cracked tooth pairs, the TVMS analytical model of the healthy tooth pairs is also established and briefly described in this section.

The physical model of the healthy tooth pair based on the slicing method is presented in Fig. 10. Excluding the influence of the edge stress concentration effect [41], the load and stiffness of each healthy slice tooth pair along TWD should be the same, as Fig. 10 (b) shows. Thus, there is no tooth torsional deformation and no coupling effect between the slices of the healthy tooth pair.
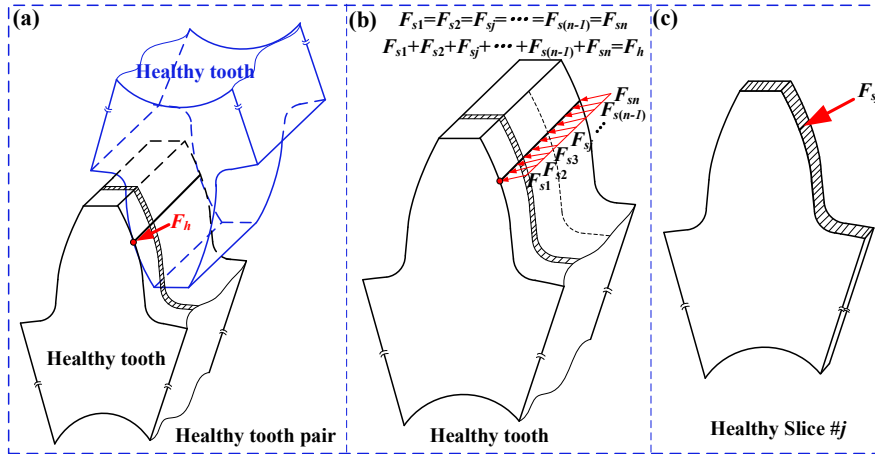

Fig. 10. Diagram of healthy tooth pair: (a) healthy tooth pair in meshing, (b) load distribution of healthy tooth, (c) healthy slice.

The parallel slice stiffness model of the tooth in the healthy tooth pair is displayed in Fig. 11. Compared to the model shown in Fig. 4, it can be found that there is no torsional deformation and no slice coupling effect in the tooth of healthy tooth pair, and its slice stiffness includes the bending stiffness k_{bhj}, shear stiffness k_{shj}, axial compression stiffness k_{ahj} and fillet foundation stiffness k_{fhj}. Hence, the stiffness of the slices of the healthy tooth can be expressed as,

$$\frac{1}{k_{t\_hj}} = \frac{1}{k_{bhj}} + \frac{1}{k_{shj}} + \frac{1}{k_{ahj}} + \frac{1}{k_{fhj}} \tag{40}$$
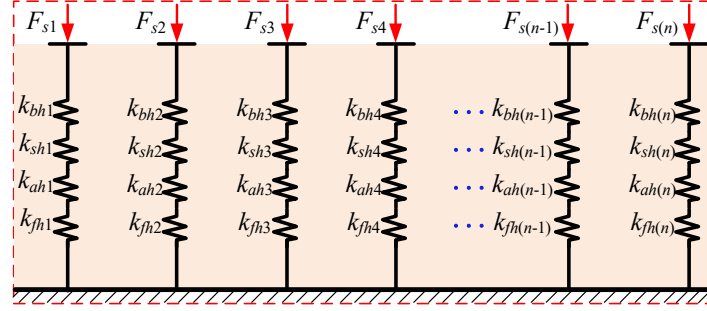
Fig. 11. Parallel slice stiffness model of the tooth in the healthy tooth pair.

The parallel slice stiffness model of the healthy tooth pair before and after deformation is also presented in Fig. 12. Due to the same stiffness and bearing load of each sliced tooth pair, the deformation of each slice is equal after the total displacement δ of the healthy tooth pair occurs. Thus, the TVMS of the jth healthy slice pair can be given as,

$$\frac{1}{k_{tp\_hj}} = \frac{1}{k_{t\_hj(p)}} + \frac{1}{k_{hj}[F_{sj}]} + \frac{1}{k_{t\_hj(g)}} \tag{41}$$

Here, subscripts (p) and (g) represent the driving and driven teeth of the healthy tooth pair, respectively.

Finally, the total TVMS $K_{h\text{-}single}$ of the single healthy tooth pair of the gear with ESC fault can be deduced as,

$$K_{h\_single} = \sum_{j=1}^{n} k_{tp\_hj} \tag{42}$$
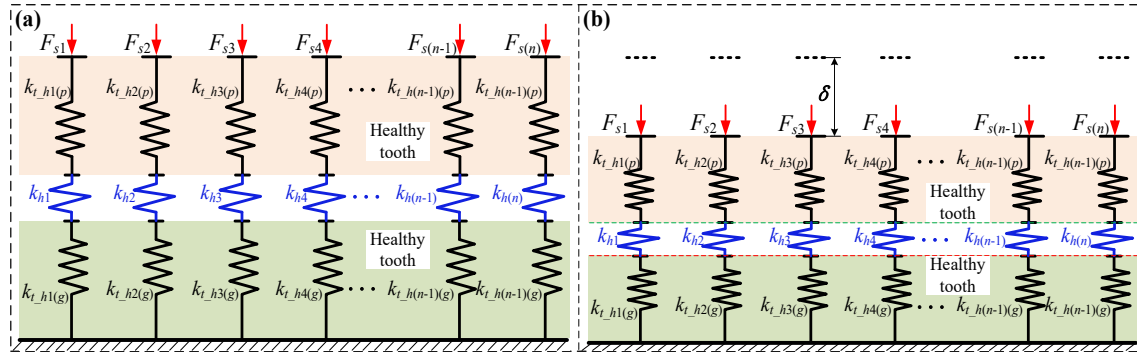
Fig. 12. Parallel slice stiffness model of healthy tooth pair: (a) before deformation, (b) after deformation.

3.3 TVMS and load distribution expressions of gear with ESC

After obtaining the analytical TVMS expressions of the tooth pair with ESC in Section 3.1 and the healthy tooth pair in Section 3.2, the expressions of the TVMS and load distribution of the gear with ESC considering ETC are developed in this section.

The flexibility of gear teeth under load in the meshing process will cause the ETC phenomenon to happen [42, 43], and then change the stiffness excitation characteristics of gears. In this paper, the effects of the ETC is also considered in the modelling for TVMS and load distributions of the gear with ESC. The TVMS of the gear with ESC considering the ETC can be expressed as,

$$K_t = \frac{F}{E_F} \tag{43}$$

Here, E_F refers to the loaded static transmission error of the gear. The ETC phenomenon usually occurs in the theoretical single-tooth engagement zone due to the larger meshing deformation of the

single meshing tooth pair. When the ETC phenomenon occurs, the loaded static transmission error can be deduced as [43],

$$E_F = \begin{cases} A = \dfrac{Q_1 Q_2 S_a + Q_2 Q_3 S_r + Q_1 Q_2 Q_3 F}{Q_1 Q_2 + Q_2 Q_3 + Q_1 Q_3}, \text{if } E_F \ge S_a \ \& \ E_F \ge S_r, \text{triple-tooth engagement} \\[4mm] B = \dfrac{Q_2 S_r + Q_1 Q_2 F}{Q_1 + Q_2}, \text{if } E_F < S_a \ \& \ E_F \ge S_r, \text{double-tooth engagement} \\[4mm] C = \dfrac{Q_2 S_a + Q_1 Q_2 F}{Q_1 + Q_2} \text{，if } E_F \ge S_a \ \& \ E_F < S_r, \text{double-tooth engagement} \end{cases} \quad (44)$$

For the case with no ETC occurs, the loaded static transmission error can be calculated as,

$$E_F = \begin{cases} \dfrac{Q_1 Q_2 F}{Q_1 + Q_2}, \text{if } E_F < S_a \ \& \ E_F < S_r \ \& \ \text{Meshing in theoretical double-tooth engagement zone} \\[4mm] Q_2 F \quad , \text{if } E_F < S_a \ \& \ E_F < S_r \ \& \ \text{Meshing in theoretical single-tooth engagement zone} \end{cases}$$

$$(45)$$

where, A, B and C mean the loaded static transmission error of the gear under three different cases of ETC shown in Eq. (44), respectively. S_a and S_r represent the backlash of the tooth pairs mesh in advance or mesh out in delay, and their derivation can be found in Ref. [43], which will not be repeated here. Q_κ means the deformation of the κth tooth pair under unit force, which is determined by the TVMS of the tooth pairs of gears with ESC, and can be expressed as,

$$Q_\kappa = \begin{cases} \dfrac{1}{K_{ec\_single}}, \text{if the } \kappa\text{th tooth pair is the tooth pair with ESC} \\[4mm] \dfrac{1}{K_{h\_single}}, \text{if the } \kappa\text{th tooth pair is healthy} \end{cases} \quad (46)$$

Considering the effects of the ETC, the load sharing factor $LSF_{tp\kappa}$ of the κth tooth pair can be finally obtained as,

$$LSF_{tp\kappa} = \frac{(E_F - E_\kappa)}{F Q_\kappa} \quad (47)$$

where E_κ represents the backlash of the κth contact tooth pair of the gear with ESC.

Thus, the meshing force of the κth meshing tooth pair can be deduced as,

$$F_\kappa = F \cdot LSF_{tp\kappa} \quad (48)$$

If the κth meshing tooth pair is the tooth pair with ESC, the total meshing force F_c of the tooth pair with ESC in Eq. (39) can be calculated by Eq. (48). In this case, the load distribution along TWD of the tooth pair with ESC can be obtained as,

$$F_{sj} = F \cdot LSF_{tp\kappa} \cdot LSF_{twj} \quad (49)$$

3.4 Proposed double-layer iterative calculation method

From the above derivation, the expressions of the slice stiffness and load distribution along TWD of the tooth pairs with ESC as well as the TVMS and load distribution between the meshing tooth pairs have been respectively established. However, the iterative calculating relationship between these parameters is still not well presented, which is also an important content of the proposed double-layer calculation model. Therefore, to reveal this coupling relationship, a double-layer iterative calculation

method for the developed analytical models is proposed in this section, in which the coupling relationships between the slice stiffness and load along TWD (inner-layer iteration), the TVMS and load distribution between the meshing tooth pairs (outer-layer iteration) are all considered. The flow chart of the proposed iterative calculation method is presented in Fig. 13.
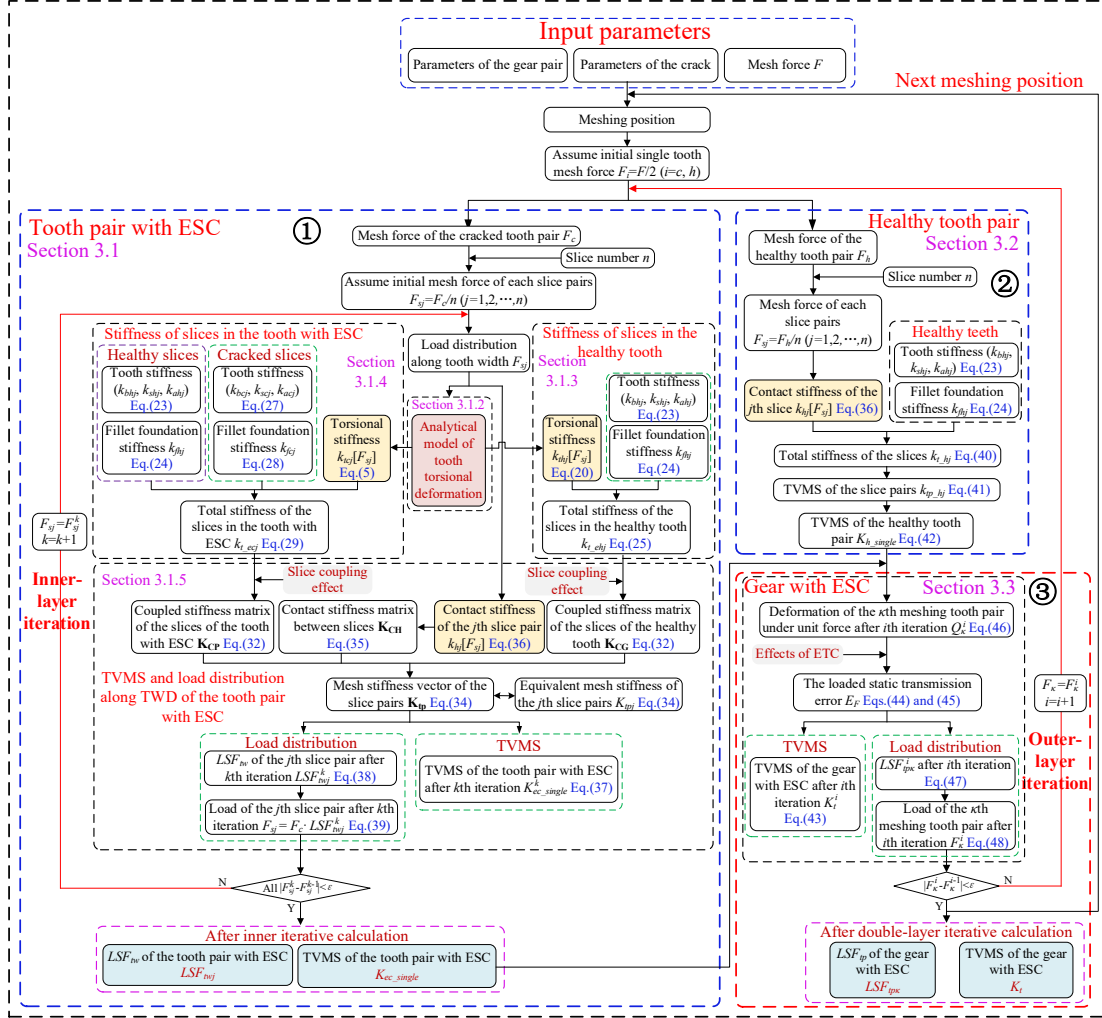

Fig. 13. Flow chart of the proposed double-layer iterative calculation method.

In Fig. 13, the blue dotted boxes with symbols ① and ② respectively represent the establishment process of TVMS modelling of the tooth pair with ESC and the healthy tooth pair, while the red dotted box with symbol ③ denotes the establishment process of TVMS and load distribution modelling of the gear with ESC based on ① and ②. In addition, the corresponding equations and chapters in the modelling process are also marked respectively in the figure. Since there are no tooth torsional deformation and slice coupling effects in the healthy tooth pair, only the coupling relationship between the stiffness and load along TWD of the tooth pair with ESC is focused on in the proposed method, that is, only the tooth pair with ESC exists inner iterative calculation.

As presented in Fig. 13, when the first iteration calculation is carried out with the meshing position determined, the initial meshing forces of the tooth pair with ESC and the healthy tooth pair are set as half of the total meshing force F respectively, and the initial distributed load of the tooth pair with ESC along TWD is set as $1/n$ of the meshing force F_c. In the inner-layer iteration shown in ①, since the tooth torsional stiffness and contact stiffness in the proposed parallel stiffness model of the tooth pairs with ESC are related to the load F_{sj}, the TVMS $K_{ec\text{-}single}$ and the load sharing factor LSF_{twj} of the tooth pair

with ESC will change after each iteration. When the iterative error of the load F_{sj} after kth inner-layer iteration is less than the allowable iterative error ε, the inner-layer iteration will exit and the TVMS $K_{ec\text{-}single}$ and the load sharing factor LSF_{twj} of the tooth pair with ESC will be obtained. Then, combined with the TVMS of the healthy tooth pairs calculated in ②, the outer-layer iteration calculation is carried out. In the outer-layer iteration shown in ③, the load sharing factors $LSF_{tp\kappa}$ between the meshing tooth pairs will be redistributed, and the TVMS of the meshing tooth pairs will be calculated again under the redistributed meshing forces. The outer-layer iteration will end until the iterative errors of meshing force F_κ after ith iteration are less than the allowable value ε and the final TVMS K_t and load distributions $LSF_{tp\kappa}$ of the gear with ESC will finally be obtained. After that, the iterative calculation for the next position will enter. The TVMS and load distributions of the gear with ESC during the whole meshing process can be finally obtained by iterative calculation at different meshing positions.

4. FE modelling for verifying the proposed analytical model

To verify the correctness and accuracy of the proposed double-layer iterative model, the FE models for calculating the TVMS and load distributions of gears with ESC are established, as shown in Fig. 14. Currently, there are two kinds of FE models widely used in the calculation of gear TVMS: the FE models with contact force and the FE models with contact element [10]. The FE model with contact force has certain limitations in considering the contact characteristics between tooth pairs, which does not meet Saint Venant's Principle. Therefore, to consider more realistic nonlinear contact characteristics between meshing tooth pairs, the FE models with contact elements are adopted in this study.
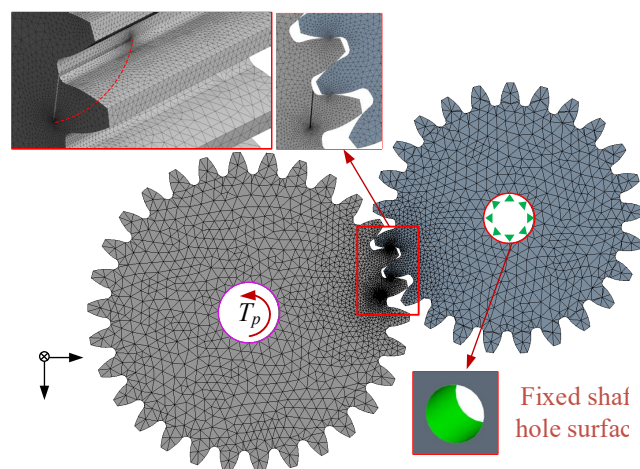

Fig. 14. FE model for calculating the TVMS and load distribution.

As Fig. 14 shows, the ESC is seeded in the driving gear. For the boundary condition setting in the FE models, the shaft hole of the driven gear is fixed, and the freedom of the shaft hole of the driving gear is constrained so that it can only rotate along the Z-axis. The torque T_p along the Z-axis is applied to the shaft hole of the driving gear, and the torsional angle $\Delta\theta_f$ along the Z-axis of the driving gear and the load distribution along the tooth with ESC are extracted. In FE calculation, the TVMS of gear under torque T_p can be calculated as [44, 45],

$$K_{t(FE)} = \frac{T_p}{\Delta\theta_f R_b^2} \tag{50}$$

The load sharing factor along TWD obtained by the FE model can be expressed as,

$$LSF_{twj(FE)} = \frac{\sigma_j \cdot S_j}{\sum\limits_{j=1}^{n}\left(\sigma_j \cdot S_j\right)} \qquad (51)$$

Here, σ_j and S_j represent the total stress and total stress distribution area of the jth tooth slice region, respectively.

5. Results and discussion

In this section, the gear pair parameters shown in Table 1 are used in the simulation of the proposed models and FE models. The correctness and accuracy of the proposed analytical model are validated by the FE results, and the influences of crack parameters and applied torque on the torsional deformation, TVMS, and load distribution characteristics of the gears with ESC are investigated and discussed. In this simulation, the slice number is set as n=20.

Table 1 Design parameters of spur gear pair used in the simulation.

| Parameter	Driving gear	Driven gear
Teeth number	30	25
Modulus m (mm)	2	2
Tooth width W (mm)	20	20
Contact ratio	1.63	1.63
Pressure angle (º)	20	20
Poisson's ratio	0.3	0.3
Young modulus E (GPa)	206.8	206.8

5.1 Analysis of verification results

To compare and analyze the differences between TVMS and load distribution calculated by the proposed model and FE models under different meshing positions, the parameters of three specific meshing positions are given in Table 2.

Table 2 Parameters of the meshing positions.

Meshing positions	Force angle α_1 (º)	Rotation angle (º)
Position A	10.27	2.94
Position B	17.13	9.80
Position C	23.98	16.65

In this comparison, the parameters of crack and torque are set as follows: q_0=4 mm, W_c=8 mm, v=15º/75º and T_p=60 N. The TVMS results calculated by the proposed, traditional and FE models under tooth crack (v=75º) and body crack (v=15º) cases are respectively compared and presented in Fig. 15. It can be seen that the traditional models, such as in Refs. [13, 14, 24, 25], will overestimate the TVMS of the gears with ESC due to ignoring the effects of tooth torsional deformation and the nonlinear contact characteristic changes caused by the NDL along TWD as well as the slice coupling effects. The TVMS results calculated by the FE and proposed models are relatively smooth in the alternating region between the single- and double-tooth engagement zones compared to the results obtained from the traditional models, which is because the effect of ETC is not considered in the traditional models. By contrast, the TVMS obtained from the proposed model are in good agreement with the FE results under both the tooth and body crack cases, which indicates the correctness and accuracy of the proposed double-layer iterative model.
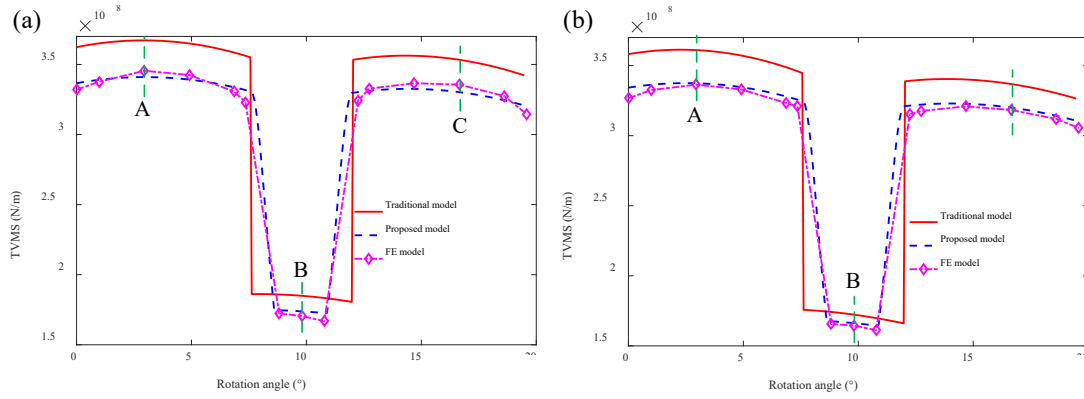
Fig. 15. TVMS comparison between different models: (a) v=15º, (b) v=75º.

To clearly present the TVMS comparison results obtained by the three models, the deviation of the proposed and traditional models from the FE model under the three meshing positions shown in Table 2 are respectively calculated and presented in Table 3. We can observe that the maximum errors between the traditional and FE models are respectively up to 8.42% and 7.59% under the body and tooth crack cases, while the maximum errors between the proposed model and FE model only separately reach 2.12% and 1.67% under the two crack angle cases, which verifies the correctness and effectiveness of the proposed double-layer iterative model.

Table 3 TVMS comparison results at three meshing positions.

Crack angle v	Models	Position A		Position B		Position C	
		TVMS ($\times 10^8$ N/m)	Error (%)	TVMS ($\times 10^8$ N/m)	Error (%)	TVMS ($\times 10^8$ N/m)	Error (%)
	FE model	3.455	-	1.706	-	3.356	-
v=15º	Traditional model	3.672	6.27	1.849	8.42	3.533	5.27
	Proposed model	3.413	-1.21	1.742	2.12	3.304	-1.54
	FE model	3.356	-	1.645	-	3.183	-
v=75º	Traditional model	3.611	7.59	1.723	4.76	3.368	5.80
	Proposed model	3.380	0.73	1.672	1.67	3.204	0.64

Fig. 16 shows the nephograms of the stress distributions of the gear pair with ESC at the three meshing positions presented in Table 2. After extracting the stress data along TWD of the tooth pair with ESC, the LSF_{tw} of the tooth pair at the three meshing positions can be calculated by Eq. (51). The LSF_{tw} of the tooth pair with ESC obtained by the FE and proposed models are compared and displayed in Fig. 17, in which the stress at the two edges of the tooth is not counted due to the edge stress concentration effect [41]. We can find that the variation trend of the load along TWD calculated by the proposed model fits well with the FE results, which also shows the correctness and accuracy of the proposed model. It should be mentioned that the calculation time of one meshing position using the proposed model only costs about 0.6 s, while it will cost about 4.5 minutes correspondingly when using FE models, which indicates the computational efficiency of the proposed model is much higher than that of the FE model.
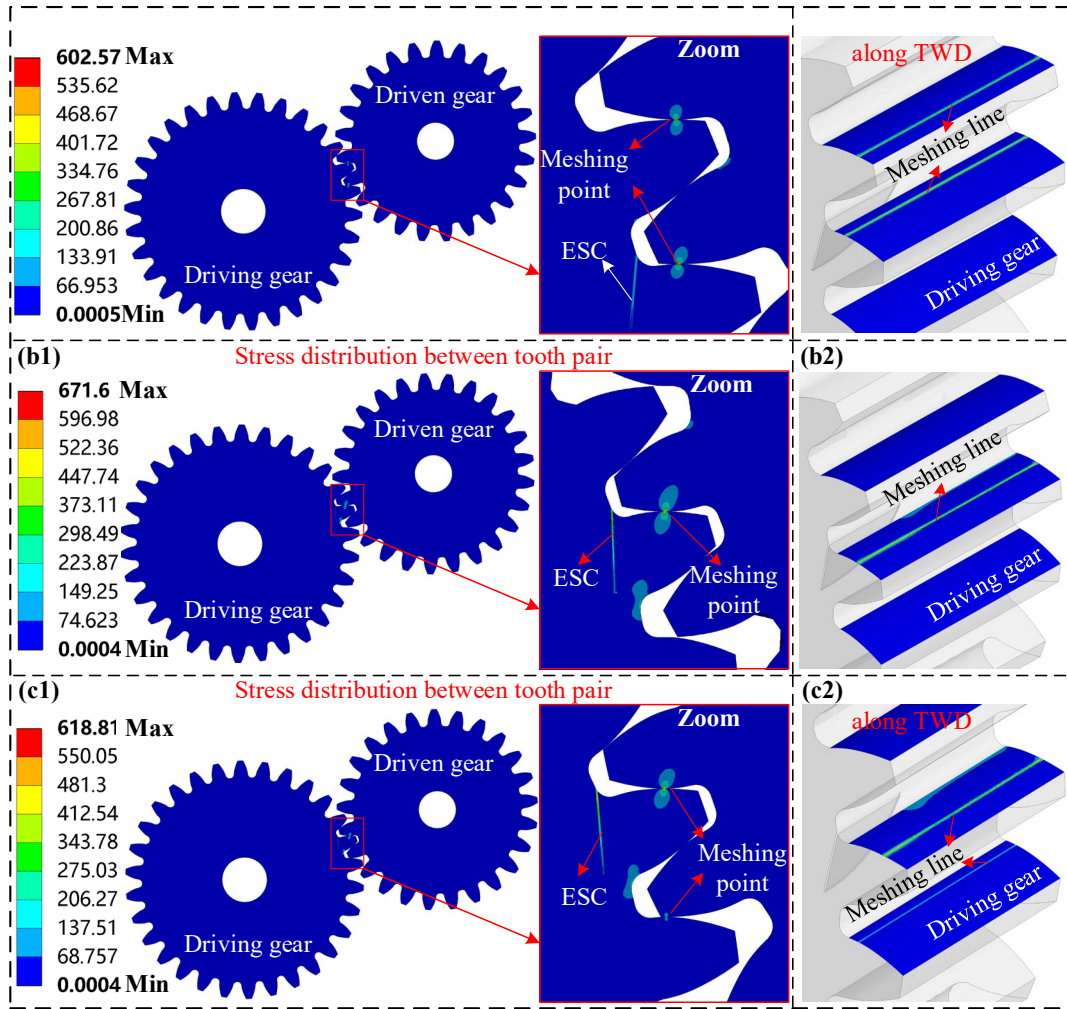
Fig. 16. Nephograms of the stress distributions of the gear pair with ESC at three meshing positions: (a) Position A, (b) Position B, (c) Position C.
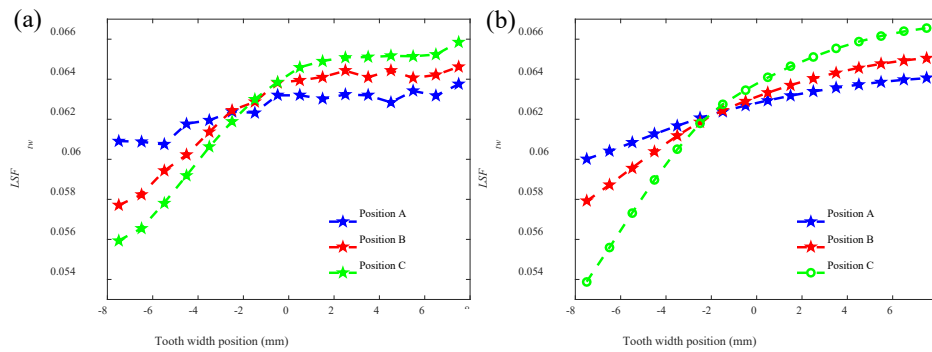

Fig. 17. Load distribution along TWD obtained by different models: (a) FE model, (b) proposed model.

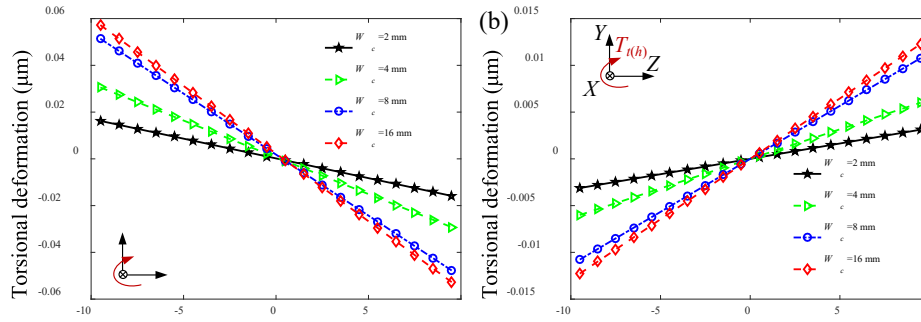## 5.2 Analysis of tooth torsional deformation of the tooth pair with ESC

Under the influence of ESC, the teeth in the tooth pair with ESC will twist, but the relationships between the direction and amplitude of the tooth torsional deformation and the ESC parameters as well as the applied torque are still unclear due to the lack of suitable analytical models. Therefore, to reveal the relationships, the effects of different crack parameters (crack length, depth and angle) and applied torque on the torsional deformation of the teeth in the tooth pair with ESC are analyzed and discussed in

this section based on the proposed model.

5.2.1 Effects of crack length W_c

The influences of crack length W_c on the torsional deformation of cracked and healthy teeth in the tooth pair with ESC is presented in Fig. 18. According to the definition of torsional deformation direction in Section 3.1.2, the torsional deformation of the stressed section of the cracked tooth shown in Fig. 18 (a) is negative on the right side of the centroid O_1 (O_1 can be seen in Fig. 6), indicating that the equivalent torque of the NDL along TWD on the left side of the centroid O_1 is greater than that on the right side, and the stressed section is rotated clockwise around the centroid O_1 in the YZ plane shown in Fig. 6 (b) under any crack length cases. This phenomenon is due to the fact that with the increase of crack length W_c, the centroid O_1 gradually deviates to the healthy slice area of the cracked tooth, which leads to the decrease of the equivalent moment caused by the distributed force on the right side of the centroid O_1 and then causes the cracked tooth turning clockwise around the centroid O_1.
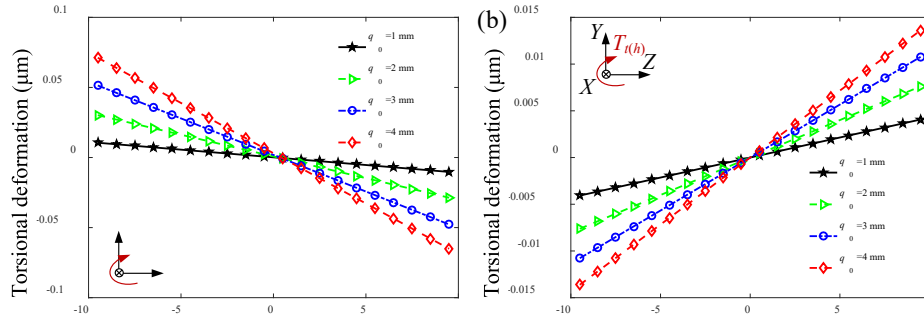

Fig. 18. Effects of crack length W_c on tooth torsional deformation ($q_0 = 3$ mm, $T_p = 60$ N, $v=15°$, Position A): (a) cracked tooth, (b) healthy tooth.

Different from the cracked tooth, the torsional deformation of the stressed section of the healthy tooth on the right side of the centroid O_3 is positive, indicating that the equivalent torque on the left side of the centroid O_3 (O_3 can be seen in Fig. 7) is smaller than that on the right side, and the stressed section also rotates clockwise around the centroid O_3 in the YZ plane. The results can be explained that the centroid O_3 of the stressed section of the healthy tooth does not shift with the change of crack length, and the distributed load on the right side of centroid O_3 is larger than that on the left side since the right side is far away from the cracked slice area, resulting in the healthy tooth turning clockwise. It can be found that the torsional deformation of both the cracked and healthy teeth gradually increases with the rise of the crack length, indicating that the crack length has a significant effect on the tooth torsional deformation amplitude of both the cracked and healthy teeth. In addition, we can see that under the same crack length, the torsional amplitude of the cracked tooth is significantly larger than that of the healthy tooth, demonstrating that the influence of centroid deviation of the stressed section caused by ESC on the tooth torsional deformation is more significant than the NDL along TWD resulted from ESC.

5.2.2 Effects of crack depth q_0

Fig. 19 displays the effects of crack depth q_0 on the torsional deformation of cracked and healthy teeth. It can be seen that the torsion direction of the stressed section of both the cracked and healthy teeth rotates clockwise around their respective centroid in the YZ plane. With the increase of crack depth q_0, the torsional deformation of both the cracked and healthy teeth in each slice position increases significantly, which is due to that the raising of crack depth q_0 leads to the more uneven distribution of the load along TWD. Similar to the effects of crack length, the torsional amplitude of the cracked tooth

is significantly larger than that of the healthy tooth under the same crack depth, which also indicates that the influence of centroid deviation of the stressed section on the tooth torsional deformation is more significant than the NDL along TWD caused by the ESC.

Fig. 19. Effects of crack length q_0 on tooth torsional deformation (W_c = 8 mm, T_p = 60 N, v=15°, Position A): (a) cracked tooth, (b) healthy tooth.

5.2.3 Effects of crack angle v

Fig. 20 shows the effects of crack angle v on the torsional deformation of cracked and healthy teeth. We can find that the torsion directions of the stressed section of both the cracked and healthy teeth rotate clockwise around their centroids in the YZ plane. The torsional deformation of the cracked tooth is still much larger than that of the healthy tooth under the same crack angle, which also shows the significant effect of centroid deviation caused by ESC on the tooth torsional deformation. With the rise of crack angle, the torsional deformation of the cracked and healthy teeth both increases, in which the increased amplitude of torsional deformation of the cracked tooth is relatively obvious, indicating that the load non-uniformity along TWD caused by the tooth crack is more significant than that caused by the body crack. This phenomenon is due to that the weakening effect of the tooth crack on the tooth stiffness is greater than that of the body crack under the same crack depth [22], which will cause the decreasing amplitude of the stiffness in the crack slice zone of the tooth with ESC is greater than that of body crack, and further lead to more uneven load distribution along TWD.
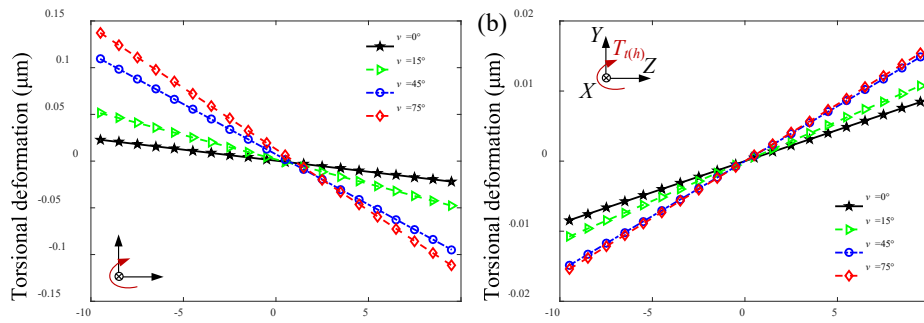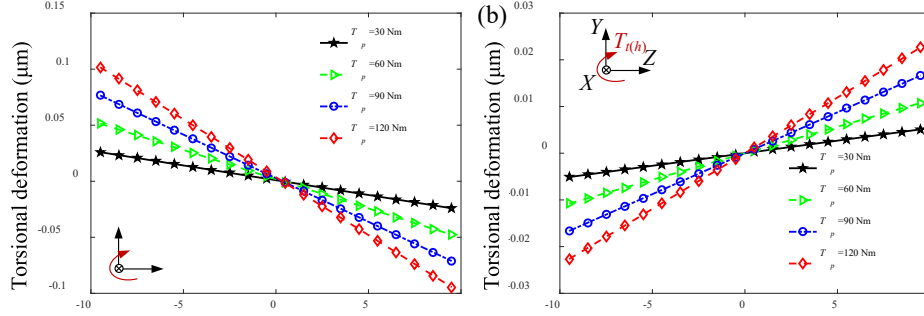

Fig. 20. Effects of crack angle v on tooth torsional deformation (W_c = 8 mm, T_p = 60 N, v=15°, Position A): (a) cracked tooth, (b) healthy tooth.

5.2.4 Effects of torque T_p

The influences of torque T_p on the torsional deformation are revealed in Fig. 21. It can be observed that the torque has no effect on the torsional direction of the stressed section, and the torsion directions of the stressed section of the teeth still rotate clockwise around their centroids. With the rise of torque, the torsional deformation of the cracked and healthy teeth increases obviously, which is due to the

positive correlation between the tooth torsional deformation and the force along TWD. Under the same torque, the torsional deformation of the cracked tooth is much larger than that of the healthy tooth, which also demonstrates that the effect of the centroid deviation of the stressed section is more significant than the NDL along TWD aroused by ESC.

Fig. 21. Effects of crack angle T_p on tooth torsional deformation ($q_0 = 3$ mm, $W_c = 8$ mm, $v=15°$, Position A): (a) cracked tooth, (b) healthy tooth.

From the above analysis in Sections 5.2.1-5.2.4, we can conclude that the increase in crack length, depth, angle and applied torque will lead to the rise of the torsional deformation of both the cracked and healthy teeth in the tooth pair with ESC. The torsional deformation direction and amplitude of the meshing teeth are mainly determined by the centroid position of the stressed section and the non-uniformity of the load along TWD caused by the ESC, in which the effects of the centroid position of the stressed section is more significant. The results also indicate the ability of the proposed torsional deformation analytical model to calculate the tooth torsional deformation at any position along TWD of gears with NDL along TWD.

5.3 Analysis of TVMS and load distributions of gear with ESC

To reveal the relationship between the TVMS, load distributions and the parameter of ESC and applied torque of the gear with ESC, the effects of the parameters of crack and applied torque on the TVMS and load distributions of the gear with ESC are simulated and studied in this section based on the proposed double-layer iterative model.

5.3.1 Effects of crack length W_c

The effects of the crack length W_c on the TVMS and load distributions of gears with ESC fault are displayed in Fig. 22. In Fig. 22 (a) and (b), the shaded parts represent the theoretical double-tooth engagement zones without considering ETC. It can be found that the ETC makes the actual double-tooth engagement zone larger and the alternating region between the single- and double-tooth engagement zones relatively smooth, but the effect of crack length on the distributions of single- and double-tooth engagement zones of the TVMS and LSF_{tp} is relatively small. From Fig. 22 (a) we can see that the crack length has a significant influence on TVMS. With the rise of crack length, TVMS gradually decreases, which is because the increase of crack length leads to the increase of the crack slice area of the tooth with ESC and then weakens the stiffness of the cracked tooth pair. Fig. 22 (b) shows the variation of load sharing factor LSF_{tp} of the tooth pair with ESC during the meshing process. It can be found that the increase in crack length will cause the LSF_{tp} of the tooth pair with ESC to decrease, which is because the TVMS decrease of the tooth pair with ESC leads to the decline of its bearing capacity.
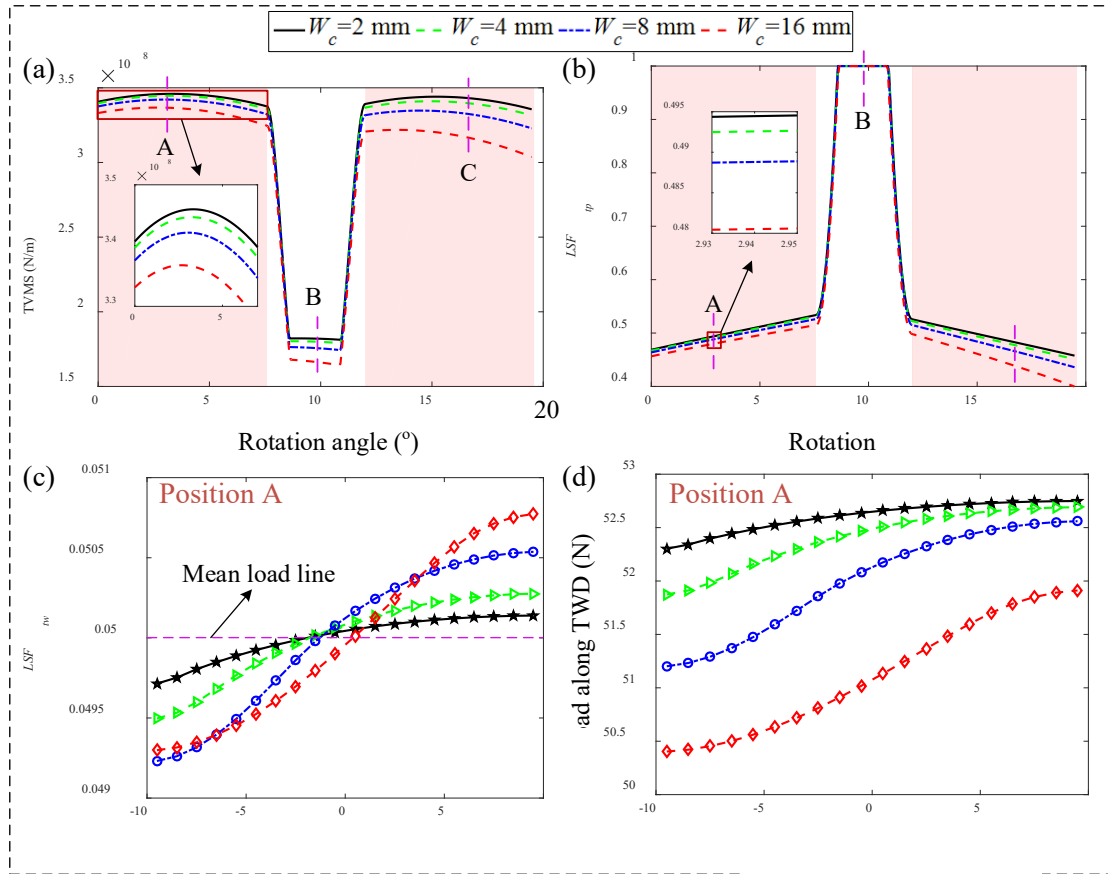
Fig. 22. Effects of crack length W_c on TVMS and load distributions ($q_0 = 3$ mm, $T_p = 60$ N, $v=15°$): (a)TVMS, (b) LSF_{tp}, (c) LSF_{tw}, (d) load along TWD.

Fig. 22 (c) presents the load sharing factor LSF_{tw} of the tooth pair with ESC at the meshing position A. The mean load line denoted by the dotted line is the theoretical LSF_{tw} of the healthy tooth pairs. It can be seen that with the increase of crack length W_c, the value difference of LSF_{tw} between the cracked and healthy slice area of the tooth pair with ESC gradually increases, that is, the curve of LSF_{tw} becomes steeper with the crack length increasing. In addition, the rise of crack length also leads to the increase of the area where the LSF_{tw} is lower than the mean load line, especially when $W_c=16$ mm,   which is due to that the increase in crack length strengthens the non-uniformity of the load along TWD. Fig. 22 (d) shows the load along TWD of the tooth pair with ESC at the meshing position A. It can be found that with the increase of W_c, the load at each slice position along TWD gradually decreases, which is because the increase of W_c leads to the obvious decrease of the meshing force of the tooth pair with ESC at position A. It can also be seen from Fig. 22 (d) that the load in the crack slice area is significantly less than that in the healthy slice area of the tooth pair with ESC, and with the increase of W_c, the load difference between the crack and healthy slice areas will increase, and the non-uniform characteristic of the load distribution along TWD will be strengthened.

5.3.2 Effects of crack depth q_0

Fig. 23 shows the effects of the crack depth q_0 on the TVMS and load distributions of gears with ESC. It can be seen from Figs. 23 (a) and (b) that the increase of crack depth q_0 will cause the decrease of the TVMS and load sharing factor LSF_{tp} of the tooth pair with ESC, which is because the increase of crack depth results in the decline of slice stiffness in the cracked slice area of the tooth with ESC. Similar to the crack length, the crack depth also has little effect on the actual distributions of single- and double-tooth engagement zones of the TVMS and LSF_{tp} when considering the ETC. Fig. 23 (c) reveals that with

the rising of the crack depth, the load sharing factor LSF_{tw} curve of the tooth pair with ESC becomes steeper, and the load distribution difference between the cracked and healthy slice areas of the tooth pair with ESC gets larger, indicating the larger crack depth will lead to the more uneven load distribution along TWD. It can be observed from Fig. 23 (d) that the increase in crack depth will lead to the overall decline of the distributed load along TWD, in which the load in the cracked slice area decreases greatly. This phenomenon can be explained that the load along TWD of the tooth pair with ESC is mainly determined by the LSF_{tp} and LSF_{tw} when the applied torque is fixed, wherein the LSF_{tp} determines the overall bearing level of the tooth pair, while the LSF_{tw} decides the distribution law of the load along TWD.
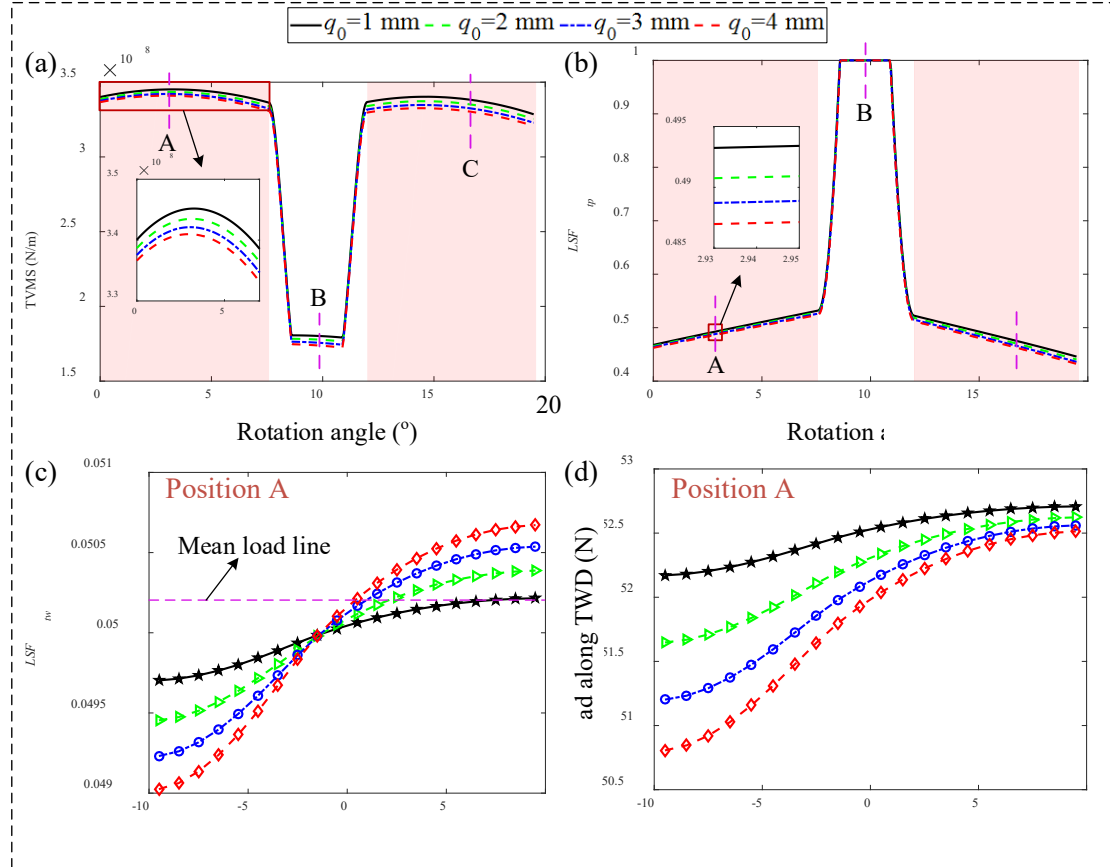
Fig. 23. Effects of crack depth q_0 on TVMS and load distributions ($W_c = 8$ mm, $T_p = 60$ N, $v=15°$): (a) TVMS, (b) LSF_{tp}, (c) LSF_{tw}, (d) load along TWD.

5.3.3 Effects of crack angle v

The influences of the crack angle v on the TVMS and load distributions of gears with ESC are presented in Fig. 24. It can be observed from Fig. 24 (a) and (b) that the increase of crack angle will cause the decrease of the TVMS and the LSF_{tp} of the tooth pair with ESC, which is due to that the stiffness weakening effect of the crack with a larger angle (tooth crack) is stronger than that with a smaller crack angle (body crack) under the same crack depth [22]. The crack angle also has little effect on the distributions of ETC zones of the TVMS and LSF_{tp}. Fig. 24 (c) and (d) show that with the rise of crack angle, the difference of load distribution between the cracked and healthy slice areas of the tooth pair with ESC gradually increases, and the non-uniformity of load distribution along TWD is strengthened. The amplitude of load along TWD at position A is mainly determined by the LSF_{tw} due to the small deviation of LSF_{tp} of the tooth pair with ESC under different crack angle cases.
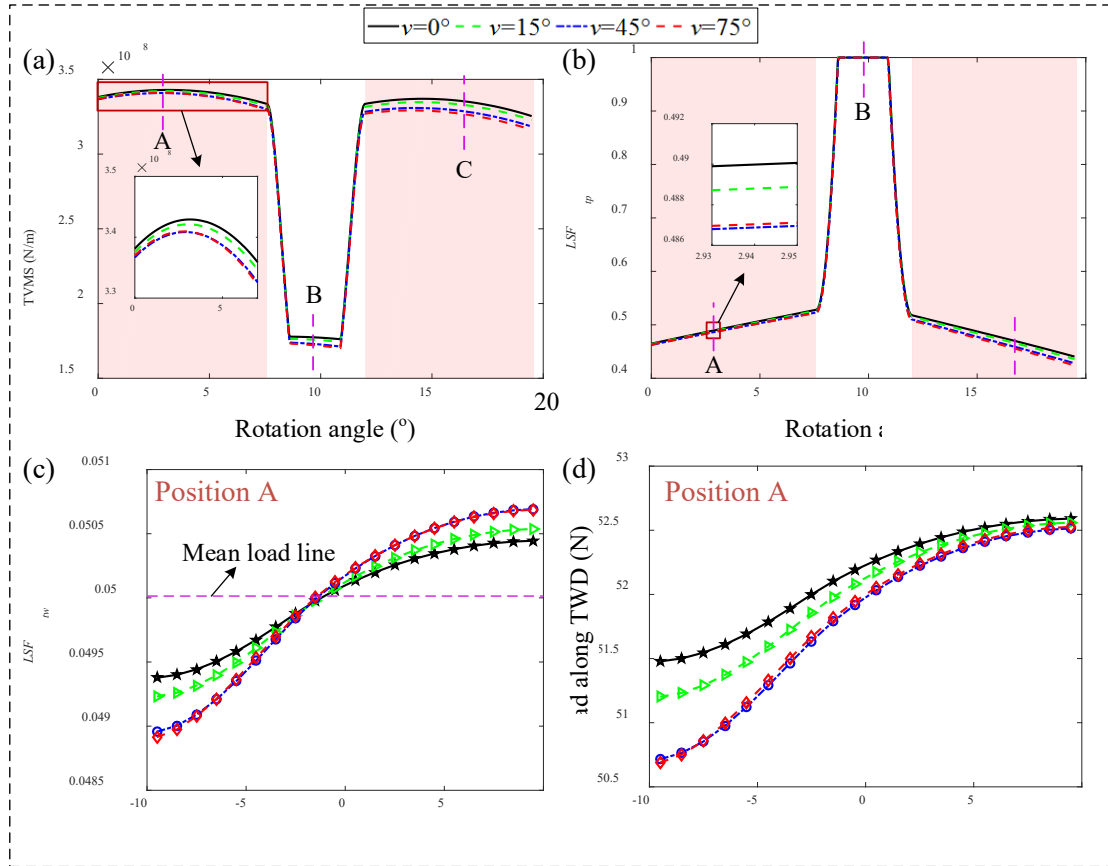
Fig. 24. Effects of crack angle v on TVMS and load distributions ($q_0 = 3$ mm, $W_c = 8$ mm, $T_p = 60$ N): (a) TVMS, (b) LSF_{tp}, (c) LSF_{tw}, (d) load along TWD.

5.3.4 Effects of torque T_p

The effects of the torque T_p on the TVMS and load distributions of gears with ESC are shown in Fig. 25. As can be found from Fig. 25 (a) and (b), the torque has a significant effect on the distributions of single- and double-tooth engagement zones of the TVMS and LSF_{tp} when considering the effects of ETC. With the increase of the applied torque, the double-tooth engagement zone of the gears becomes larger, which is because the larger torque leads to the larger deformation of the meshing tooth pair and prolongs the engagement time of the tooth pair meshing in advance or out in delay. In Fig. 25 (a), we can see that the increase of torque T_p will result in the increase of TVMS, which can be explained that there is a nonlinear relationship between the tooth contact stiffness and contact force, and the larger meshing force will cause the nonlinear growth of contact stiffness, then lead to the increase of TVMS [32-34]. From Fig. 25 (b) we can find that the applied torque mainly affects the LSF_{tp} of the cracked tooth pair during the ETC zones, and for other engagement zones, its effect is relatively small. This phenomenon can be explained that the increase of torque will also lead to the increase of the TVMS of the healthy meshing tooth pair due to the nonlinear characteristics of the contact stiffness, and its increased amplitude almost keeps the same with the cracked tooth pair during the non-ETC zones, while in the ETC zones, the deviation between the nonlinear contact stiffness of the healthy and cracked tooth pairs gradually grows larger due to the larger difference of meshing force between the two meshing tooth pairs.
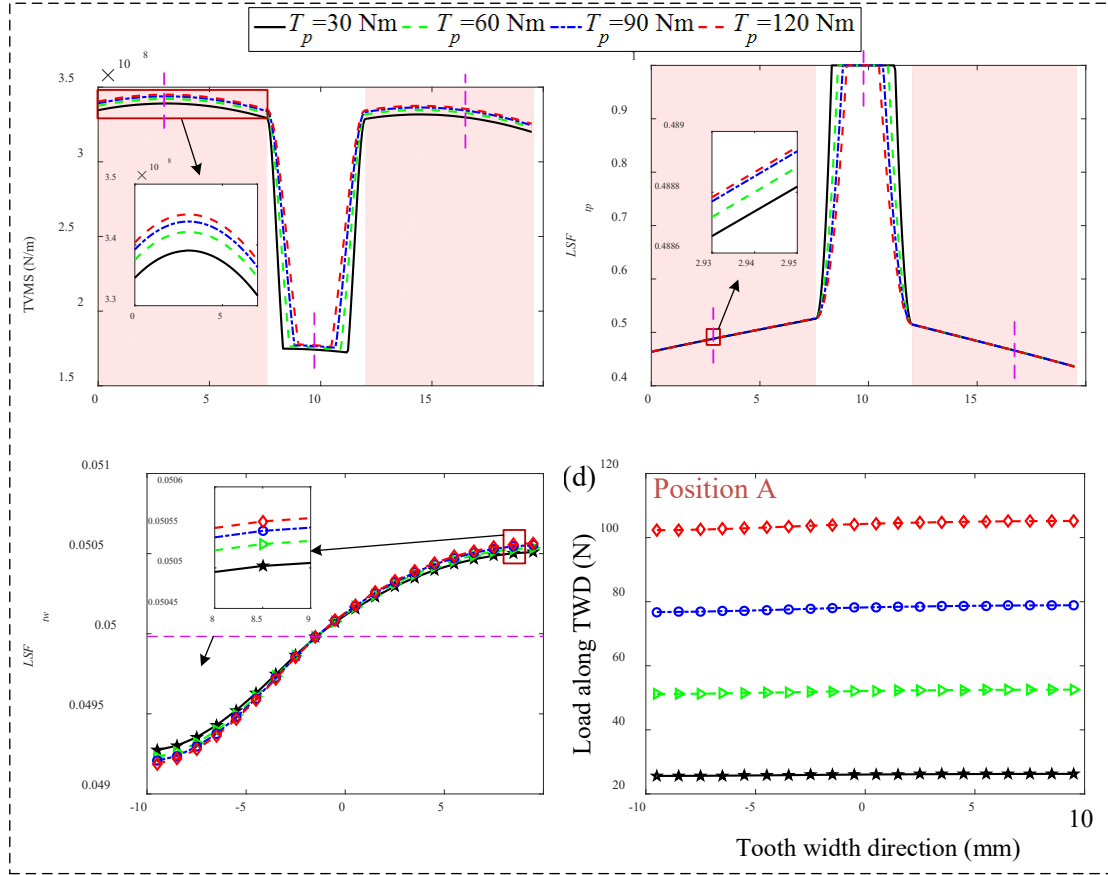
Fig. 25. Effects of torque T_p on TVMS and load distributions ($q_0 = 3$ mm, $W_c = 8$ mm, $v=15°$): (a) TVMS, (b) LSF_{tp}, (c) LSF_{tw}, (d) load along TWD.

Fig. 25 (c) shows that with the increase of torque, the curve of load sharing factor LSF_{tw} of the cracked tooth becomes steeper, but this effect is relatively small compared to the effects of crack parameters. The small difference of LSF_{tw} under different torque is mainly due to the different torsional stiffness of the slices and slice coupling stiffness caused by different torques. In Fig. 25 (d), with the increase of torque, the overall level of the load along TWD increases significantly, but the load distribution law along TWD keeps close. This phenomenon is due to that the total meshing force of the tooth pair with ESC increases significantly with the increasing of torque, while the influences of torque on the load sharing factors LSF_{tp} and LSF_{tw} are limited at position A.

From the above analysis in Sections 5.3.1-5.3.4, it can be concluded that with the increase of the length, depth and angle of the ESC, the TVMS and the total bearing load of the tooth pair with ESC will decrease, and the non-uniformity of the load along TWD will be strengthened, leading to the decline of the load on the cracked slice area of the tooth pair with ESC. Due to the nonlinear contact characteristics, the increase of applied torque will result in the increase of TVMS, but the effects of torque on the LSF_{tp} and LSF_{tw} of the tooth pair during the meshing zones without ETC are relatively small and can be ignored. The crack parameters have less influence on the TVMS and LSF_{tw} in the ETC zone, but the effect of the torque is relatively significant. The load distribution along TWD of the tooth pair with ESC is mainly determined by the applied torque, the LSF_{tp} as well as the LSF_{tw}, in which the applied torque and LSF_{tp} mainly determine the overall bearing level of the tooth pair, and the LSF_{tw} of the tooth pair mainly determines the distribution law of the load along TWD. The results validate the ability of the proposed double-layer iterative analytical model to express the relationship between the TVMS and load

distributions of gears with ESC under different ESC and applied torque parameters.

6. Conclusions

To understand the unclear coupling mechanism between TVMS and load distribution along TWD of gears with ESC, a double-layer iterative analytical model for the TVMS and load distributions of the gear with ESC is proposed in this paper. In the proposed model, an analytical model of tooth torsional deformation and a parallel slice stiffness model of the tooth pair with ESC as well as a double-layer iterative calculation method for the TVMS and load distributions are included and developed separately. The proposed double-layer iterative analytical model is validated to have the ability to realize the accurate and fast decoupling calculation of the TVMS and load distributions of gears with ESC, and its calculation speed is about 450 times faster than that of the FE model. Through the proposed double-layer iterative model, we can evaluate the tooth torsional deformation, TVMS and load distributions between meshing tooth pairs and along TWD of gears with ESC under different ESC and applied torque parameters. The proposed model can also be used for the modelling of TVMS and load distributions of gears with asymmetric errors or faults along TWD.

It should be noted that some future study works are worthy being carried out based on the proposed model in this paper. For example, by considering the structure coupling effect of the fillet foundation between the neighbouring teeth [46, 47] under the effects of NDL along TWD, the influences of manufacturing errors [48], installation errors [28, 49] and tooth modification errors [27, 50], the proposed analytical model can be further extended and improved.

Appendix A. Stiffness calculation parameters of the slices of the healthy tooth

In Eqs. (21) and (24) in Section 3.1.3, parameters d_1, x_1, d_2, I_{hx} and h_1 are respectively expressed as follows:

$$d_1 = \begin{cases} R_b[(\alpha_1 + \alpha_2)\sin\alpha_1 + \cos\alpha_1 - \cos\alpha_2], & \text{if } R_b > R_g \\ R_b[(\alpha_1 + \alpha_2)\sin\alpha_1 + \cos\alpha_1] - R_g\cos\theta_f, & \text{if } R_b \leq R_g \end{cases} \tag{A.1}$$

$$x_1 = \begin{cases} R_b[(\alpha + \alpha_2)\sin\alpha + \cos\alpha - \cos\alpha_2], & \text{if } R_b > R_g \\ R_b[(\alpha + \alpha_2)\sin\alpha + \cos\alpha] - R_g\cos\theta_f, & \text{if } R_b \leq R_g \end{cases} \tag{A.2}$$

$$d_2 = \begin{cases} R_b\cos\alpha_2 - R_g\cos\theta_f, & \text{if } R_b > R_g \\ 0, & \text{if } R_b \leq R_g \end{cases} \tag{A.3}$$

$$I_{hxi} = \begin{cases} \dfrac{1}{12}h_{hx1}{}^3 W_j, & i = 1 \\ \dfrac{1}{12}h_{hx2}{}^3 W_j, & i = 2 \end{cases}, \quad A_{hxi} = \begin{cases} h_{hx1} W_j, & i = 1 \\ h_{hx2} W_j, & i = 2 \end{cases} \tag{A.4}$$

$$h_1 = R_b[(\alpha_1 + \alpha_2)\cos\alpha_1 - \sin\alpha_1] \tag{A.5}$$

In Eq. (A.4), the height h_{hxi} of the micro-section at position x_i can be calculated as,

$$h_{hxi} = \begin{cases} 2R_b[(\alpha + \alpha_2)\cos\alpha - \sin\alpha], & i = 1 \\ 2R_b\sin\alpha_2 + 2r\left[1 - \sqrt{1 - \left(\dfrac{x_2}{r}\right)^2}\right], & i = 2 \end{cases} \tag{A.6}$$

Here, r represents the radius of the transition curve between the tooth profile and the dedendum circle.

Appendix B. Stiffness calculation parameters of the slices of the tooth with ESC

The parameters in Eq. (27) in Section 3.1.4 are derived as follows,

$$d_3 = q\cos\nu + R_g\cos\theta_f - R_g\cos\varphi \tag{B.1}$$

$$\begin{cases} I_{cxi} = \dfrac{1}{12}h_{cxi}{}^3 W_j \\ A_{cxi} = h_{cxi}W_j \end{cases}, \quad i=1,2,3 \tag{B.2}$$

$$h_{cxi} = \begin{cases} \dfrac{1}{2}h_{hx1} + h_r + \dfrac{R_a\cos\alpha_K - R_g\cos\theta_f - d_2 - x_1}{R_a\cos\alpha_K - R_g\cos\theta_f + d_3}\left(R_g\sin\varphi - q\sin\nu - h_r\right), \ i=1 \\ R_b\sin\alpha_2 + r\left[1 - \sqrt{1 - \left(\dfrac{x_2}{r}\right)^2}\right] + h_r + \dfrac{R_a\cos\alpha_K - R_g\cos\theta_f - d_2 + x_2}{R_a\cos\alpha_K - R_g\cos\theta_f + d_3}\left(R_g\sin\varphi - q\sin\nu - h_r\right), \ i=2 \\ \sqrt{x_3{}^2 + |MB|^2}, \ i=3 \end{cases} \tag{B.3}$$

$$h_{F(xi)} = \begin{cases} h_1 + \dfrac{1}{2}h_{hx1} - \dfrac{1}{2}h_{cx1}, \ i=1 \\ h_1 + R_a\sin\alpha_2 + r\left[1 - \sqrt{1 - \left(\dfrac{x_2}{r}\right)^2}\right] - \dfrac{1}{2}h_{cx2}, \ i=2 \\ |DC|\cos(\alpha_1 + \theta) - |OC|, \ i=3 \end{cases}$$

$$\text{(B.4)}$$

$$l = |DC|\sin(\alpha_1 + \theta) \tag{B.5}$$

In Eq. (B.5), $|DC|$ and θ can be deduced as,

$$|DC| = \sqrt{\left(\dfrac{|GH| + |GB|\tan\theta}{\tan\theta + \tan\alpha_m} + h\right)^2 + \left(\dfrac{-\tan\alpha_m(|GH| + |GB|\tan\theta)}{\tan\theta + \tan\alpha_m} + |GH| - d_1 - d_2\right)^2} \tag{B.6}$$

$$\theta = \arctan\left(x_3 / |MB|\right) \tag{B.7}$$

of which,

$$|MB| = R_g\sin\theta_f + \dfrac{R_g\sin\varphi - q\sin\nu - h_r}{R_a\cos\alpha_K - R_g\cos\theta_f + d_3}\left(R_a\cos\alpha_K - R_g\cos\theta_f + x_3\right) + h_r \tag{B.8}$$

In Eq. (28), parameters $s_f{}'$ and $u_f{}'$ can be given as,

$$S_f{}' = |BQ| = \sqrt{d_3{}^2 + \left(R_g\sin\varphi - q\sin\nu + R_g\sin\theta_f\right)^2} \tag{B.9}$$

$$\mu_f{}' = \left[\dfrac{1}{2}S_f{}' + \sqrt{\left(\dfrac{|GH| + |GB|\tan\gamma}{\tan\gamma + \tan\alpha_1} - |GB|\right)^2 + \left(\dfrac{-\tan\alpha_1(|GH| + |GB|\tan\gamma)}{\tan\gamma + \tan\alpha_1} + |GH|\right)^2}\right]\tan(\alpha_1 + \gamma) \tag{B.10}$$

Here,

$$|GH| = |O_1H| - |O_1G| = R_b / \cos\alpha_1 - R_g \cos\theta_f \qquad (B.11)$$

$$|GB| = R_g \sin\theta_f$$

(B.12)

Acknowledgements

Data availability

The datasets generated and analyzed during the current study are available from the corresponding author upon reasonable request.

Declaration of Competing Interest

The authors declare that they have no competing financial interests or personal relationships that could have appeared to influence the work reported in this paper.

References

[1] X. Liang, M. Zuo, Z. Feng. Dynamic modeling of gearbox faults: A review. Mech. Syst. Sig. Process, 2018, 98: 852-876.

[2] Y. Lei, L. Jing, M. Zuo, Z. He. Condition monitoring and fault diagnosis of planetary gearboxes: A review. Measurement, 2014, 48(1): 292–305.

[3] D. G. Lewicki, R. Ballarini. Gear crack propagation investigations. NASA technical report ARL-TR-957, 1996.

[4] A. Stenberg, H. Holttinen. Analysing failure statistics of wind turbines in Finland. EWEC2010.

[5] Y. Yang, N. Hu, C. Zhe, H. Jiao, Z. Lun. Improved Mesh Stiffness Method and Vibration Analysis of a Planetary Gear System with a Spatial Tooth Crack. MACHINES, 2022; 10(12): 1168.

[6] S. Wu, M. J. Zuo, A. Parey. Simulation of spur gear dynamics and estimation of fault growth. J. Sound Vib. 2008; 317 (3–5): 608–624.

[7] Chaari F, Fakhfakh T, Haddar M. Analytical modelling of spur gear tooth crack and influence on gear mesh stiffness. Eur J Mech – A/Solids 2009; 28: 461–8.

[8] D. G. Lewicki. Effect of rim thickness on gear crack propagation path. J. Mech. Des. 1997; 119:88–95.

[9] S. Zouari, M. Maatar, T. Fakhfakh. Following Spur Gear Crack Propagation in the Tooth Foot by Finite Element Method. J Fail. Anal. and Preven. 2010; 10: 531–539.

[10] H. Ma, J. Zeng, R. Feng, P. Xu, B. Wang, B. Wen. Review on dynamics of cracked gear systems. Eng. Fail. Anal. 2015; 55: 224–245.

[11] Z. Chen, J. Zhang, W. Zhai, Y. Wang, J. Liu. Improved analytical methods for calculation of gear tooth fillet-foundation stiffness with tooth root crack. Eng. Fail. Anal. 2017; 82: 72–81.

[12] X. H. Tian. Dynamic Simulation for System Response of Gearbox Including Localized Gear Faults. University of Alberta, Edmonton, Alberta, Canada, 2004 (Master's Thesis).

[13] O. D. Mohammed, M. Rantatalo, J. O. Aidanpaa. Improving mesh stiffness calculation of cracked gears for the purpose of vibration-based fault analysis, Eng. Fail. Anal. 2013; 34: 235–251.

[14] Z. G. Chen, W. M. Zhai, Y. M. Shao, et al. Analytical model for mesh stiffness calculation of spur gear pair with non-uniformly distributed tooth root crack. Eng. Fail. Anal. 2016; 66: 502–514.

[15] H. Ma, R. Song, X. Pang. Time-varying mesh stiffness calculation of cracked spur gears. Eng Fail Anal. 2014; 44: 179–94.

[16] Y. Shao, Z. Chen. Dynamic features of planetary gear set with tooth plastic inclination deformation due to tooth root crack. Nonlinear Dyn 2013; 74: 1253–1266.

[17] Z. Wan, H. Cao, Y. Zi. An improved time-varying mesh stiffness algorithm and dynamic modeling of gear-rotor system with tooth root crack. Eng. Fail. Anal. 2014; 42:157–77.

[18] X. Liang, M. Zuo, M. Pandey. Analytically evaluating the influence of crack on the mesh stiffness of a planetary gear set. Mech. Mach. Theory. 2014; 76:20–38.

[19] X. Zhou, Y. Shao. Time-varying meshing stiffness calculation and vibration analysis for a 16 degree of dynamic model with linear crack growth in a pinion. J. Sound Vib. 2012; 134: 011011.

[20] H. Ma, X. Feng, R. Song, J. Yang. Time-Varying Mesh Stiffness Calculation of Spur Gears Based on Improved Energy Method. Journal of Northeastern University (Natural Science). 2014; 35(6): 863.

[21] L. Yang, L.Wang, Y. Shao, C. K. Mechefske, Q. Chen. A new calculation method for tooth fillet foundation stiffness of cracked spur gears. Eng. Fail. Anal. 2021, 121(3): 105173.

[22] L. Yang, L.Wang, Y. Shao, F. Gu, A. Ball, D. Mba. Dynamic modelling and analysis of cracked gear system with tip relief based on proposed variable-angle deformation energy integration method. Nonlinear Dynamics. 2022; 111(5): 4141-4172.

[23] K. Chen, Y. Huangfu, Z. Zhao, H. Ma, X. Dong. Dynamic modelling of the gear-rotor systems with spatial propagation crack and complicated foundation structure. Mech. Mach. Theory. 2022; 172: 104827.

[24] Z. Chen, Y. Shao. Dynamic simulation of spur gear with tooth root crack propagating along tooth width and crack depth. Eng. Fail. Anal. 2011; 18:2149–2164.

[25] O. Mohammed, M. Rantatalo, J. Aidanpaeae. Vibration signal analysis for gear fault diagnosis with various crack progression scenarios. Mech. Syst. Sig. Process, 2013; 41(1-2): 176–195.

[26] Y. Yang, W. Xia, J. Han, Y. Song, J. Wang, Y. Dai. Vibration analysis for tooth crack detection in a spur gear system with clearance nonlinearity. Int. J. Mech. Sci. 2019; 157–158: 648–661.

[27] Z. Sun, S. Chen, Z. Hu, X. Tao. Improved mesh stiffness calculation model of comprehensive modification gears considering actual manufacturing. Mech. Mach. Theory. 2022; 167: 104470.

[28] Q. Wang, K. Xu, T. Huai, H. Ma, K. Wang. A mesh stiffness method using slice coupling for spur gear pairs with misalignment and lead crown relief. Applied Mathematical Modelling. 2021; 90: 845–861.

[29] L. Han, H. Qi. Influences of tooth spalling or local breakage on time-varying mesh stiffness of helical gears. 2017; 79: 75–88.

[30] S. Wang, R. Zhu. Vibration-Based Fault Diagnosis of Helical Gear Pair With Tooth Surface Wear Considering Time-Varying Friction Coefficient Under Mixed Elastohydrodynamic Lubrication Condition. 2022; 144(7): 071603.

[31] A. Saxena, A. Parey, M. Chouksey. Effect of shaft misalignment and friction force on time varying mesh stiffness of spur gear pair. Engineering Failure Analysis. 2015, 49: 79–91.

[32] L. Yang, Q. Zeng, H. Yang, L. Wang, G. Long, X. Ding, Y. Shao. Dynamic characteristic analysis of spur gear system considering tooth contact state caused by shaft misalignment. Nonlinear Dyn., 2022; 109: 1591–1615.

[33] M. Sánchez, M. Pleguezuelos, J. Pedrero. Approximate equations for the meshing stiffness and the load sharing ratio of spur gears including hertzian effects. Mech. Mach. Theory. 2017; 109: 231–249.

[34] Z. Cao, Z. Chen, H. Jiang. Nonlinear dynamics of a spur gear pair with force-dependent mesh stiffness. Nonlinear Dyn. 2020; 99: 1227–1241.

[35] D. Yang, J. Lin. Hertzian damping, tooth friction and bending elasticity in gear impact dynamics. Journal of Mechanisms, Transmissions, and Automation. 1987; 109(2): 189–196.

[36] X. Tian. Dynamic Simulation for System Response of Gearbox Including Localized Gear Faults. University of Alberta, Edmonton, Alberta, Canada, 2004 (Master's Thesis).

[37] P. Sainsot, P. Velex, O. Duverger. Contribution of gear body to tooth deflections – a new bidimensional analytical formula. Journal of Mechanical Design –ASME. 2004; 126(4): 748–752.

[38] W. Wang, W. Hu, N. Armstrong. Fatigue crack prognosis using Bayesian probabilistic modelling. Mechanical Engineering Journal, 2017; 4 (5): 16-00702-16-00702.

[39] L. Yang, L. Wang, W. Yu, Y. Shao. Investigation of tooth crack opening state on time varying meshing stiffness and dynamic response of spur gear pair. Eng. Fail. Anal. 2021; 121(8): 105181.

[40] Y. Huangfu, K. Chen, H. Ma, X. Li, H. Han, Z. Zhao. Meshing and dynamic characteristics analysis of spalled gear systems: A theoretical and experimental study. Mech. Syst. Sig. Process. 2020, 139: 106640.

[41] W. Yu, C. Mechefske. A New Model for the Single Mesh Stiffness Calculation of Helical Gears Using the Slicing Principle. Iran. J. Sci. Technol. Trans. Mech. Eng. 2019; 43: S503–S515.

[42] H. Ma, X. Pang, R. Feng, R. Song, B. Wen. Fault features analysis of cracked gear considering the effects of the ETC. Eng. Fail. Anal. 2015; 48: 105–20.

[43] H. Ma, J. Zeng, R. Feng, X. Pang, B. Wen. An improved analytical method for mesh stiffness calculation of spur gears with tip relief. Mech. Mach. Theory. 2016; 98: 64–80.

[44] X. Liang, H. Zhang, M. Zuo, Y. Qin, Three new models for evaluation of standard involute spur gear mesh stiffness, Mech. Syst. Sig. Process. 2018; 101: 424–434.

[45] Y. Luo, N. Baddour, M. Liang. A shape-independent approach to modelling gear tooth spalls for time varying mesh stiffness evaluation of a spur gear pair. Mech. Syst. Sig. Process. 2019; 120(APR.1): 836–852.

[46] C. Xie, L. Hua, X. Han, J. Lan, X. Wan, X. Xiong. Analytical formulas for gear body-induced tooth deflections of spur gears considering structure coupling effect. Int. J. Mech. Sci. 2018; 148: 174–190.

[47] J. Ning, Z. Chen, Y. Zhi, X. Hua, W. Zhai. Improved analytical method for gear body-induced deflections with tooth root crack considering structural coupling effect. Engineering Failure Analysis. 2022, 137: 106400.

[48] L. Yang, Q. Chen, L. Yin, L. Wang, Y. Shao. Dynamic characteristic of spur gear system with spalling fault considering tooth pitch error. Qual. Reliab. Engng. Int. 2021: 17028391.

[49] Z. Liu, Y. Huangfu, H. Ma, Z. Peng, J. Zhu, H. Wang, Z. Li. Traveling wave resonance analysis of flexible spur gear system with angular misalignment. Int. J. Mech. Sci. 2022; 232: 107617.

[50] S. Ye, S. Tsai. A computerized method for loaded tooth contact analysis of high-contact-ratio spur gears with or without flank modification considering tip corner contact and shaft misalignment. Mech. Mach. Theory. 2016; 97: 190–214.